Fully printable integrated multifunctional sensor arrays for intelligent lithium-ion batteries

Nuo Sun[1,2,10], Qinlang Rong[1,2,10], Jie Wu[3], Liting Huang[2], Stefano Passerini ®[4], Hong Li ®[5], Hailong Wang[1], Jing Chen[1], YongAn Huang ®[6] ✉, Zhimeng Liu ®[1], Linyu Hu[2], Kang Xu[7] ✉, Yuanjing Lin ®[2,8,9] ✉ & Xin He ®[1,3] ✉

Monitoring battery health states and predicting potential hazards are crucial technologies for ensuring the safe operation of battery packs. Current battery risk control often lacks indicators and timeliness for the accidents due to complexity in convoluted and distinct electrochemical behaviors of diverse cell chemistries. Here, we enable lithium-ion batteries with intelligence by integrating a conformal array of multifunctional sensors into the packing foil. Fully printed sensing arrays are prepared by nano-fabricating process with sensing inks, provide advantages with minimized weight increase (49 mg), strong resilience against multi-dimensional disturbances, and long-term stability as integrated system. Operando thermal, mechanical, and chemical features serve as quantitative indicators of degradation across various issues, including over-dis/charging, low-temperature/high-rates Li-plating, internal-short circuit, breakage or thermal abuse, ensuring safety with a lead time. Additionally, sensors for flammable gases and electrolyte leakage directly trigger alarms upon real-time analysis, efficiently providing warnings in complex situations. As important advance in intelligent energy storage management, this platform can be applied universally to various battery-types or pack-levels.

Efficient and reliable energy management is essential for the universal application of rechargeable batteries in various scenarios. Since its birth in early 1990s, lithium-ion batteries (LIBs) have revolutionized our daily energy usage over the last few decades, penetrating personal electronics and communications, to large-scale grid-storage, and to the electrification of diversified transportation means, including vehicles, aircrafts, railway, and cargo ships[1–3]. However, the LIBs used in these scenarios, often in huge packs ranging from $10^3 \sim 10^6$ watt-hours (Wh), also bring serious challenges in operational safety. Particularly when LIBs with aggressive electrode materials are subjected to abusive working conditions, such as extreme temperatures, mechanical pressure, and vibration, or fast discharge and charge[4]. These abusive conditions induce heterogeneities, including Li⁺ concentration gradients, Li-plating on graphite surface, parasitic reactions, and

continuous growth of solid-state electrolyte interphase (SEI) at the expense of irreversible consumption of both Li^+ inventory and electrolytes. Thus, the cell reactions are forced to deviate severely from the designed electrochemical pathways and leads to sustained performance degradation as well as unpredictable catastrophic outcomes[5,6]. These safety challenges highlight the urgent need for accurate and real-time monitoring, assessment, and estimation of state of health (SOH) down to the battery chemistry level, so that the internal changes and aging of battery components could be detected in a timely manner for early warning. Generally, the multivariate degradation mechanisms involved in batteries frequently stem from intrinsic heterogeneities, which are further accumulated due to the complex cycling conditions. Such nano-scale degradations could lead to rapid capacity fading, mechanical failure (serious bulge, breakage for gas and electrolyte leaking), or even thermal runaway (fire and explosion). Therefore, deterioration raises urgent demand on an effective solution for assessment, which would be multifunctional sensor arrays that capable to capture multiple relevant descriptors simultaneously. Such arrays should be fully integrated into the batteries with minimal weight and footprints, and operated on the basis of highly efficient intelligent system.

Several monitoring techniques have been developed to evaluate the state of the battery. Optical fiber offers advantages in measurement accuracy[7–11], which is suitable for laboratory-research on fundamental mechanisms with the reliance on highly precise and complicated decoding devices[12,13]. The acoustic technique enables highly sensitive and non-invasive detection by measuring the propagation velocity and amplitude attenuation of acoustic waves through the cell body[14,15]. However, the size of detection equipment is hard to be deployed on each cell along with its service lifetime[13]. In addition, fundamental research on single factor of the battery may oversimplify the real-life scenarios where only "big data" collected from a large number of cells could carry statistical significance. More importantly, despite the mature sensory technologies, their integration into battery always casts significant impact on energy density and cycling stability of battery[16], cost of fabrication, and energy consumption for on-site sensing[12,13], as well as signal drifting and crosstalk due to the variation of local conditions[17–19]. Thus, developing multifunctional sensing array that can be conformally integrated within the cells as tattoo manner would be significant to realize multiple key features tracking for intelligent battery health status analysis with negligible impact on battery operation.

In this work, we report a mechanically flexible, stretchable, ultrathin, conformal, and anti-interference sensing array, that can be integrated with LIBs and operated by distributed artificial intelligence system. The multifunctional sensing array is seamlessly printed into the packing foil that seals the cell, providing a nonintrusive solution for simultaneous and selective screening on battery management as an integrated intelligent sensing array system (IISAS). As shown in Fig. 1a, this platform serves as quantitative indicators for comprehensive real-time flow analysis via distributed artificial intelligence. It achieves comprehensive assessment on the routine behaviors for state estimation by deep-learning algorithm, and also faults-diagnosis (over-charging and over-discharging, low-temperature failure, internal short circuits, mechanical and thermal runaway) with degradation insights from Li-plating, cell-bulging, and overheating. Moreover, warning alarm is directly activated with the detection of flammable gas (hydrogen (H_2) gas, dimethyl carbonate (DMC) vapor) and electrolyte leaking in sufficient advances for safety evacuation, which renders the battery management systems into artificial intelligent to enhance robustness under complex situations. The reliable functionalities of IISAS rely on the extracted features from temperature, pressure, strain, H_2 gas, DMC vapor, and liquid electrolyte sensor (Fig. 1b). By combining additive and subtractive manufacturing processes in printable tattoo manner, the design of embedded sensing arrays compromises

the conflict between effective monitoring battery health status and interfering their electrochemical performance[8,11,16]. While the weight and space footprints of integrated sensors is minimized, and signal accuracy and sensor durability against external interferences are heightened due to proximity to the cell body. The transmission loss of thermal and mechanical sensing signals with gradients is reduced, and noise signals from device vibrations can be filtered[13,20]. By further integration with optimized sensing signals processing circuit design (Fig. 1c, d), the signals are finely resolved within the analog-to-digital converter (ADC) and wireless transmitted via Bluetooth through the microcontroller unit (MCU) for further decoded based on intelligent algorithms. The as-fabricated IISAS bridges the existing technology gap between reliable battery features extraction and real-time states assessment. Such highly integrated intelligent LIBs provide advantages in terms of highly reliability, cost-effectiveness, real-time monitoring, and smart analyzing, which are critical for practical scenarios where large-format ($> 10^3$ Wh) LIBs are required. Moreover, the proposed device fabrication and system integration approach reported here offers desirable transferability and compatibility to a variety of battery form factors and chemistries, encouraging further deployment as a universal tool in practical applications.

Results

Fabrication of multifunctional sensing arrays

The fabrication process of the multifunctional sensing array is illustrated in Supplementary Fig. 1a. CO_2 laser generator is utilized to scribe on the hybrid-based outer layer of the aluminum (Al)−polymer foil used to package pouch cell. The pattern of grooves follows the designed interconnects of sensors with an etched depth of 20 μm. Laser etching provide space and weight for sensing array fabrication with minimized impact on energy density and electrochemical performance of batteries. Additionally, the accuracy and durability of sensing array is improved through the embedded design in the PET layer, as shown in Supplementary Fig. 1d, e. The printed sensing array embedded in the Al-polymer packing foil substrate conforms with the curved shape of the cell, making them capable of accommodating the swelling and contraction of pouch cells at intervals during the cycling. Such close contact between the sensors and cell body also contributes to the miniremized transmission gradient and eliminates the non-uniformity pressure-induced deformation, which is crucial to prevent tip discharge in cell body during the electrochemical process[21]. The grooves are further cleaned and polished with anhydrous ethanol and ultraviolet ozone, followed by plasma and UV-light treatment applied to enhance the surface wettability. The sensors electrode patterns and interconnects are firstly screen printed with conductive silver (Ag), which is adhered closely to the hybrid substrate without heterogeneous junction gap, are shown in Supplementary Fig. 2. The sensitive materials of the sensors are then printed into the patterned electrode grooves via drop-coating of custom synthesized inks. Details of sensors manufacturing process are described in "Methods". Lastly, the isolating and hydrophobicity polyurethane (PU) film is attached as the outmost packaging layer to ensure the sustainable operation of sensors against deterioration, oxidation, and moisture immersion. Notably, the encapsulation layer for gas sensors requires effective breathability, thus, the waterproof and breathable polytetrafluoroethylene (PTFE) film is adopted. For the rapid absorption of liquid electrolyte, the porous and hydrophobic polyvinylidene fluoride (PVdF) serves as a hydrophobic intermedia. For comparison, commercially available thermistor, pressure sensor, and strain gauge are also attached to the surface of pouch cell, as illustrated in Supplementary Figs. 1b and 3. Printed sensing array shows obvious advantages in terms of weight increasement and space occupancy compared to commercial sensors. The total increased weight of the embedded sensing array with interconnects is merely 0.049 g, which is negligible when compare to the weight of commercial sensors (1.762 g,

Supplementary Fig. 1c) or cell body (22.348 g), especially when the cell is in large format. Meanwhile, the space footprint of printed sensing array is only 16.844 mm³. This fabrication process could easily adapt to various battery configurations and packing, with sensor types and quantities being tailored based on the requirements in various application scenarios. More importantly, printed sensor arrays offer strong stability against various interferences (Supplementary Fig. 5) compare to commercial sensors, which are hard to couple with the thermal and mechanical changes of cell due to the electrochemical process.

The schematic illustration for the positioning of sensors in the pouch cell is shown in Fig. 1b. Besides their functionalities, the location of each sensor is highly dependent on the representative features it is designed to extract. The temperature sensor is positioned 2 cm below the positive electrode tab, which usually experiences the highest temperature rise on the plane[22]. The strain sensor stays at the center of the pouch cell, where the most noticeable mechanical stress occurs[23]. The pressure sensor is placed in the central area of the negative electrode side, because preferential Li-plating would occur there[24], providing rich information for internal pressure changes against the fixture. Electrolyte leakage frequently occurs at points where the packing foil and electrode tabs make contact, as these structural

points exhibit reduced strength, which accelerates packaging aging and compromises seals. Thus, liquid sensor is strategically placed in proximity of the electrode tabs. Both the H_2 gas and DMC vapor sensors are also placed close to the sealing area to detect gaseous leakage with rapid response. Such arrangement of sensors optimizes operando monitoring efficiency for efficient and comprehensive feature extraction.

Data processing and analysis with the intelligent system

The multifunctional real-time sensing signals are subsequently transduced, amplified, filtered, and transmitted via the PCB (Fig. 1c, d), and further integrated with the commercialized battery management system (BMS) for decoding. The system block diagram of the PCB, along with the circuit diagram of the analog signal conditioning module is illustrated in Supplementary Fig. 4a, b, respectively. Intelligent algorithms are configured either in the cloud or on-site for data mining based on leveraging factors, such as feature extraction from collected datasets, available computing resources, and the associated costs of data transmission and storage. The establishment of a distributed artificial intelligence system operation and maintenance technology, known as cloud-edge collaboration, enables SOH analysis, fault
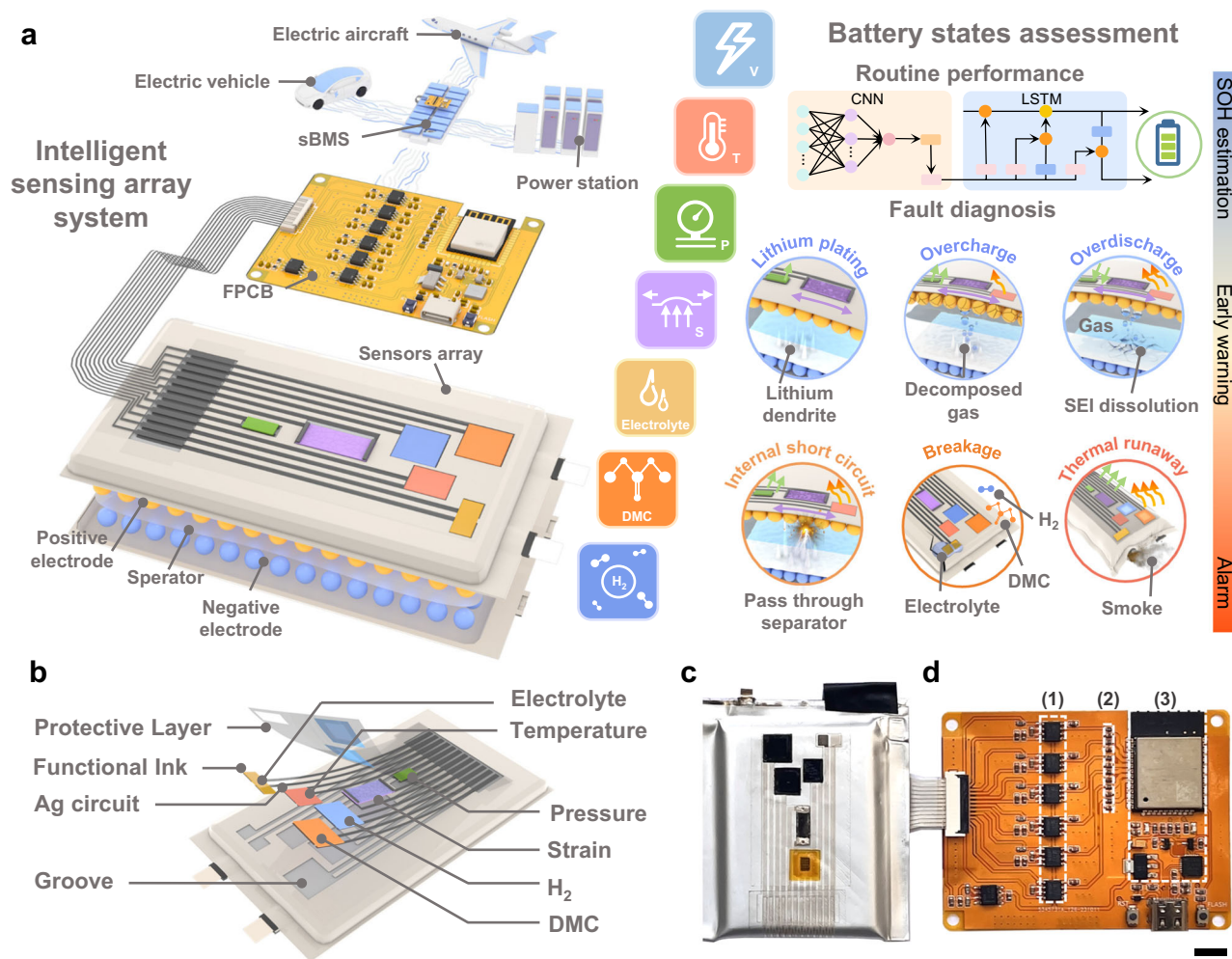

Fig. 1 | Schematic illustration and actual images of the IISAS with multi-feature analysis for battery state self-assessment. a Schematic of the exploded three-dimensional model of the layer-by-layer assembly of sensors array (including temperature, pressure, strain, electrolyte liquid, H_2 gas, and DMC vapor sensor), and the application on routine performance estimation and fault diagnosis (Li-plating, over-charging, over-discharging, internal short circuit, breakage, and thermal runaway). **b** Schematic for the positional arrangement of fully printed sensors on the integrated intelligent pouch cell with the configuration of embedded sensor arrays at each layer. **c, d** Photograph of **c** integrated intelligent LIBs (Scale bar, 1 cm) and **d** custom designed printed circuit board (PCB) (All photographs in this paper were taken by the authors). The white dashed boxes indicate the locations of (1) amplifier, (2) low-pass filter, and (3) integrated circuit components.
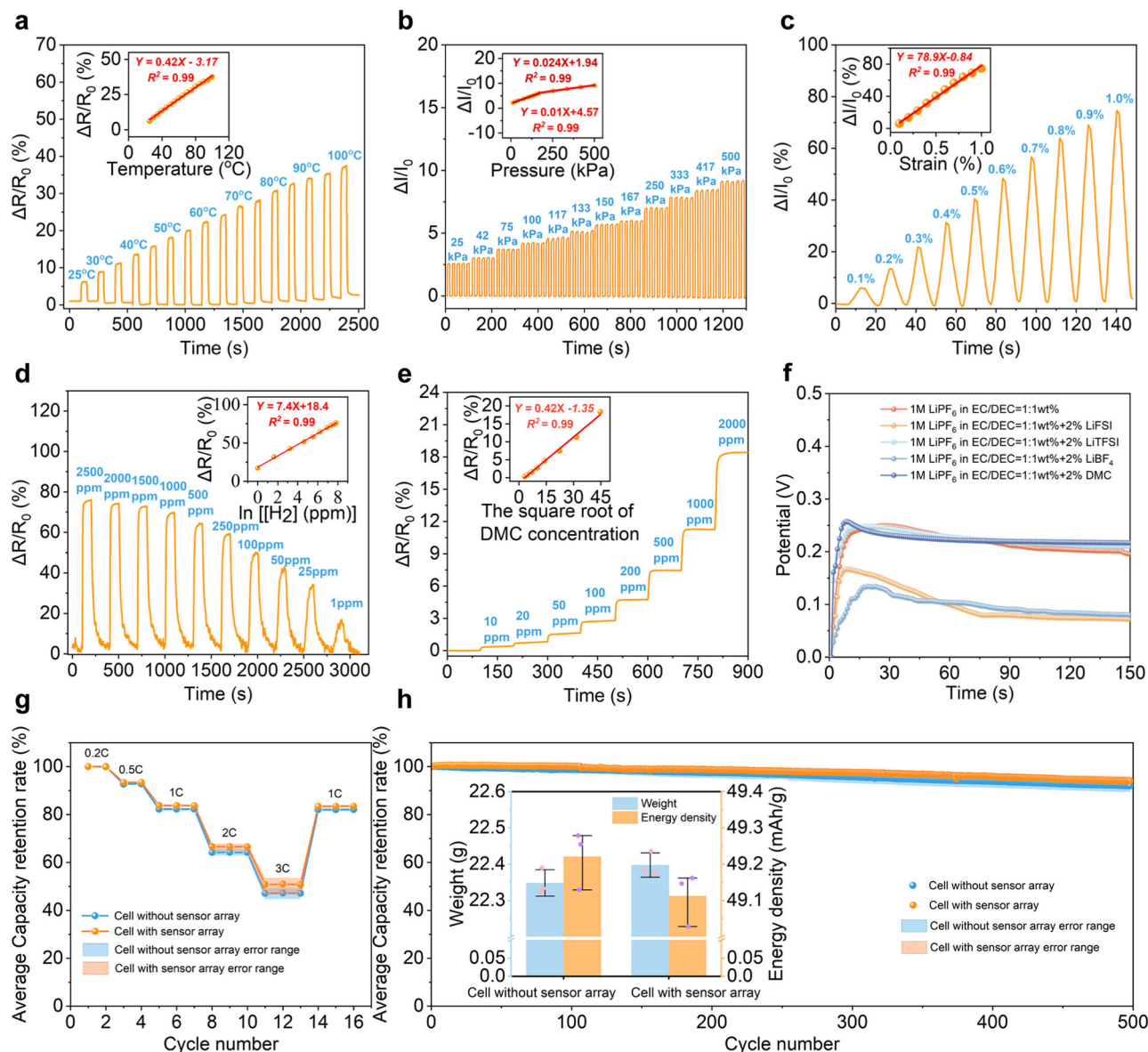
Fig. 2 | Experimental characterizations of the fully printed multifunctional sensors. a Resistance response of temperature sensors in the range of 20–100 °C. **b** Current response of the pressure sensor in the range of 25.0–500.0 kPa. **c** Current response of the strain sensor in the range of 0.1–1.0%. **d** Resistance response of H_2 gas sensors with the concentration from 1 ppm to 2500 ppm. **e** Resistance response of DMC vapor sensor with the concentration from 10 ppm to 2000 ppm. Insets in (**a**–**e**) show the corresponding calibration plots of the sensors. **f** Open circuit potential response of the electrolyte leakage sensor (0.1 μL of 1 M $LiPF_6$ in EC/DEC 1:1 wt% and with 2% additives of lithium difluorosulfonylimide (LiFSI), lithium bis(trifluoromethanesulfonyl)imide (LiTFSI), lithium tetrafluoroborate ($LiBF_4$) salt or DMC solvent). **g, h** Averaged **g** rate capability and **h** cycling stability of pouch cells with and without sensor array after normalization. The inset is the comparison of the weight and energy density of pouch cells with and without sensors array (Data are presented as mean values ± SD).

identification, and alarm activation through mechanism-data fusion. This enables comprehensive and early identification through the tracking of corresponding evolution processes, which holds promise to the revolution of traditional and generalized fault warning systems.

Sensors performance characterization

The performance of each individual sensor is evaluated separately before integration for multi-signal analysis. The independent operating conditions for multifunctional sensing arrays are integrated via electrical decoupling to ensure reliable extraction of representative features for each cell. Figure 2a displays the resistance (R) responses of the temperature sensor based on MXene ($Ti_3C_2T_x$, $T_x = F, O, OH$) and poly(3,4-ethylenedioxythiophene) polystyrene sulfonate (PEDOT: PSS) to match the temperature within the range of 20–100 °C. The detailed materials characterization with SEM/EDS images are shown in

Supplementary Fig. 6. The high-sensing efficiency is based on the negative temperature coefficient of resistance (TCR), as illustrated in Supplementary Fig. 7a. Both MXene and PEDOT: PSS in temperature sensing film exhibit negative TCR. The rising temperature activates electrons to hop from the valence band to the conduction band, resulting in more charge carriers to generate thermal activation current[25]. The functional groups in poly(vinyl alcohol) (PVA) prevent slippage of the stacked MXene against mechanical deformation induced signal crosstalk. A linear relationship between the change rate of resistance and temperature (°C) is fitted in the inserted figure of Fig. 2a, with a sensitivity of approximately 0.42% per degree Celsius (normalized to the resistance at 20 °C). The response time of the temperature sensor in IISAS is 9 s (Supplementary Fig. 7b), and it remains consistent with changes in the commercial temperature sensor (Supplementary Fig. 5a), suggesting an efficient and precise

detection. The sensor also demonstrates higher stability against mechanical and chemical interferences than commercial sensor, such as being stretched up to 8%, and squeezed with 200 N (Supplementary Fig. 5d–g). In addition, it also shows advantages when bent to 90° with temperature changes of 30 °C, under 200 N at 50 °C, hammered repeatedly, sharp temperature changes from −45 °C to 100 °C, exposed to 2000 ppm H_2 gas and 2000 ppm DMC vapor, and immersed into corrosive electrolyte that has been known to consist of trace amount of HF and other acidic species (Supplementary Fig. 7c–h). Such rapid response, strong stability, and high accuracy ensure the much higher sensing accuracy than conventional BMS against conventional volume changes or even under battery fault conditions.

Differing from the temperature sensors, the active material ink used for both the pressure and strain sensors is optimized to perform close to zero TCR[26]. The active material ink has a maximum resistance fluctuation rate of less than 2.5% with temperature from 20 °C to 80 °C (Supplementary Fig. 8). The pressure sensor in current application detects the pressure difference between external applied pressure and self-generated internal pressure, achieving a sensitive response along the vertical axis (Supplementary Fig. 9). The strain sensor measures expansion with heterogeneous wrinkle-type deformation, which is prepared by spraying zero TCR ink as a plating layer on the insulated PDMS film (Supplementary Fig. 12). The preparation processes of pressure and strain sensors are shown in Supplementary Figs. 10 and 13. More details for the working mechanisms of the pressure and strain sensors are illustrated in Supplementary Figs. 11a and 14a, respectively. The pressure sensor works effectively in the range of 25.0–500.0 kPa (Fig. 2b) with a response/recovery time within 0.9 s under the pressure of 200.0 kPa (Supplementary Fig. 11b). In addition, the pressure sensor demonstrates high accuracy (Supplementary Fig. 5b), and stronger anti-interferences against temperature and strain changes (Supplementary Fig. 5h–k) than the commercial one. It also displays strong resistivity against chemical interferences (Supplementary Fig. 11c–e). And it maintains superior recoverability and stability even after 30000 cycles under 200.0 kPa (Supplementary Fig. 11f, g). Figure 2c displays the performance of strain sensor with an expansion range of 0.1–1.0%. The response/recovery time is controlled within a short term of 0.3 s (Supplementary Fig. 14b). It performs precise strain detection (Supplementary Fig. 5c), and demonstrates stronger adaptability as well as resistivity against temperature and pressure interferences (Supplementary Fig. 5l–o) than the commercial sensor. It also displays high resistivity against chemical interferences (Supplementary Fig. 14c–e). More importantly, the strain sensor provides consistent detection with frequence from 0.6 to 2.0 Hz and precise results even after 2500 cycles under 1.0% strain (Supplementary Fig. 14f, g). Given that thermal and mechanical features contain rich information regarding how the electrochemical process departs from the designed pathways, collecting precise datasets without imposing a high burden on the complex decoupling analysis could significantly improve the accuracy of status assessment and estimation.

Gas and electrolyte leakage sensors are particularly valuable for confirming cell integrity and activating warning alarm. Detection of gaseous species for battery SOH monitoring encounter the critical challenge on their detection limit, especially in ambient at room temperature. Figure 2d, e illustrate the representative resistance responses of the H_2 gas and the DMC vapor sensor, measured via chrono amperometry with relevant concentrations of H_2 in the ranges of 1–2500 ppm and DMC vapor in 10–2000 ppm, respectively. The sensitive ink of H_2 gas sensor comprises a nano-sized tin dioxide (SnO_2)- palladium (Pd)- molybdenum disulfide (MoS_2) (Supplementary Fig. 15) via the functioning of semiconductors[27]. The Pd-nanoparticles capture diatomic H_2 and dissociate it to single H-atom, and then the single H-atom undergoes redox reaction with oxygen on the surface of

SnO_2-MoS_2, leading to an increased electron density with decreased resistance (Supplementary Fig. 16a). The DMC vapor sensor is prepared by in-situ polymerization of phthalocyanine nickel (NiPPc) on the multi-wall carbon nanotubes (MWCNT) host as NiPPc/MWCNT composite (morphological and chemical details are shown in Supplementary Figs. 17 and 18). It enables the detection of DMC vapor in air, and has advantages of well-performed durability against humidity and volume changes of substrate. The working mechanism of DMC vapor sensor bases on the transmittivity of electrons in the sensitive layer[28] (Supplementary Fig. 19a), where the NiPPc local coordination structure has a reduced local electron density due to the appearance of C = O bond in absorbed DMC vapor (Supplementary Fig. 20). This allows the universal application of such sensors for batteries that contain esters in electrolytes, which are the indispensable ingredients in mainstream LIB powered devices. Both the H_2 gas and DMC vapor sensor provide fast response rate under regular air atmospheric conditions at 25 °C, which achieves a t_{90} values of 16 s at 25 ppm H_2 and 10 s at 100 ppm DMC vapor (Supplementary Figs. 16b and 19b). These gas sensors present high selectivity among volatile solvents, and capable to maintain highly repeatability and stability during the long-term operation of LIBs. (Supplementary Figs. 16c–i and 19c–h).

The electrolyte leakage sensing relies on the potential difference between Ag-AgCl double electrodes, and the top-view and cross-sectional image of sensor is shown in Supplementary Fig. 21. The presence of porous PVdF coating layer (Supplementary Fig. 22) effectively protects sensor from aqueous solution, and facilitates electrolyte absorption (Supplementary Fig. 23a, b). Figure 2f shows the open circuit voltage of electrolyte leakage sensor activated by different electrolyte compositions. The detection limit for leakage of 0.1 μL electrolyte reaches a t_{90} time within 4 s, and provides precise potential signals under the mechanical and chemical interferences Supplementary Fig. 23c–g). As the temperature increases, the response time becomes shorter due to the faster molecular dynamics (Supplementary Fig. 23h). The reproducibility of these six sensors is shown in Supplementary Fig. 24.

Figure 2g, h demonstrate the influence of sensing array on the electrochemical performance in terms of rate capability and cycling stability. The percentage of capacity retention is calculated based on an averaged result of 3 cells after normalization, which show nearly identical trends with or without the sensor array. Slightly improvements at high current rates could be attributed to the thermal effect of sensing array (the infrared (IR) images are shown in Supplementary Fig. 25a), whereas the frequence of dataset capture could be adjusted by MCU on controlling heat release. For the long-term cycling stage, cells with and without sensing array perform same capacity fading rate, indicating that the impact on cycling stability of cell can be negligible. Moreover, as shown in Supplementary Fig. 25b, the ratio of PCB power consumption to battery capacity is 4.755 mAh (0.43% of total energy) with cable and 5.558 mAh (0.51% of total energy) with Bluetooth at a frequency of 0.1 Hz, respectively, which allows sufficient datasets collection with minimized energy consumption. The inserted figure in Fig. 2h shows the impact of sensors array on the weight and the energy density of 1.1 Ah pouch cell. The printed sensors array introduces a total increase on the 0.23% of weight, but the reduction of the energy density is merely 0.22%, which is negligible for commercial cells at similar level or even larger format.

State estimation and self-assessment

The structural degradation of the LIBs is presented in the form of electrical, mechanical, and thermal behaviors, which can be quantified for state assessment, estimation, and decision-making. Signals collected by IISAS are integrated with the voltage signal from BMS, providing comprehensive information throughout the lifetime of LIBs. As the proof-of-concept shown in Fig. 3a, the voltage (V), temperature (T), pressure changes in MPa (ΔP), and strain changes in % (ΔS) datasets
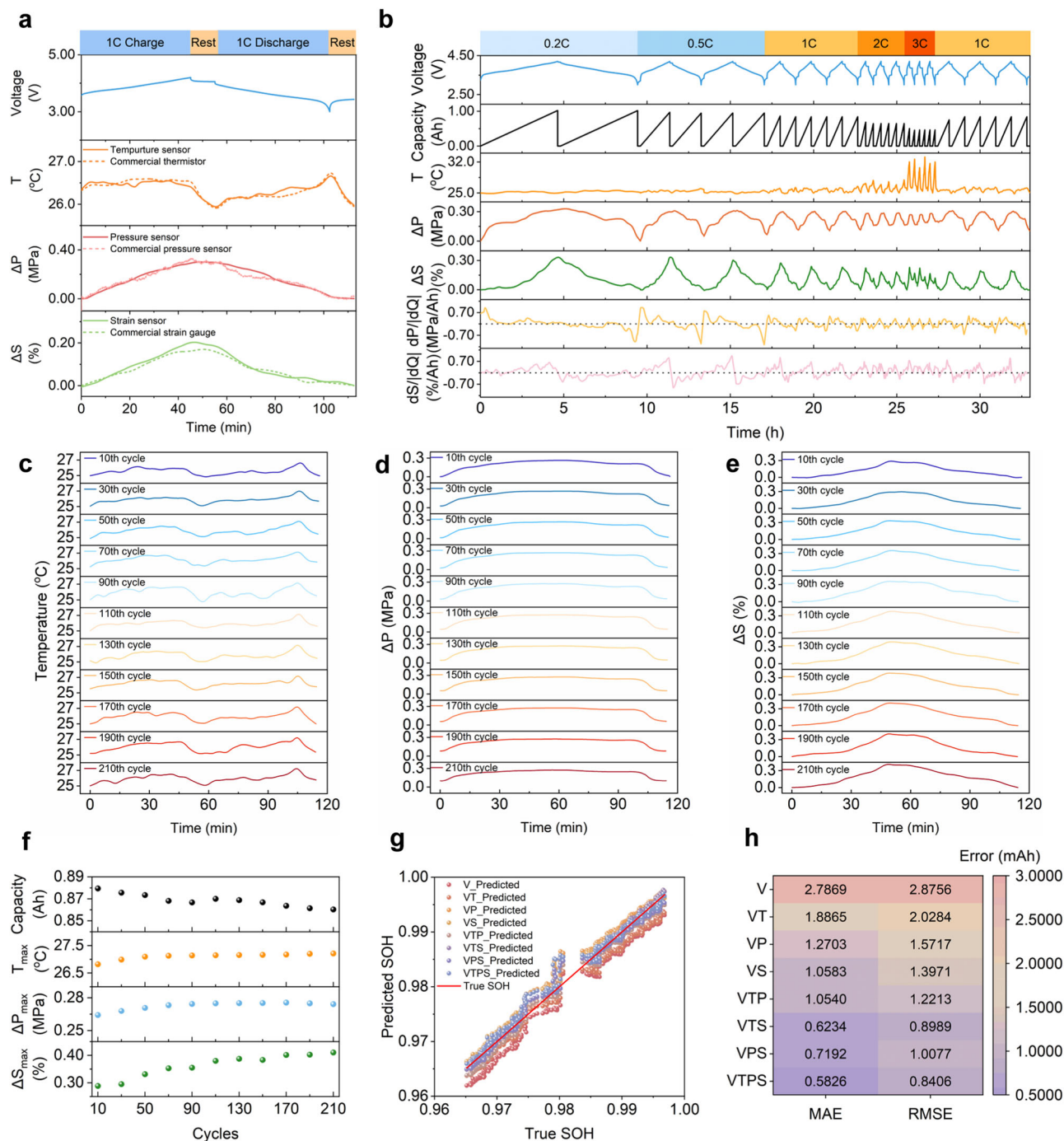
Fig. 3 | Operando monitoring of battery states during cycling and SOH estimation. a Variation of voltage, T, ΔP, ΔS signals for an intelligent pouch cell (1.1 Ah) for charging and discharging at 1 C collected by IISAS and commercial sensors under 25 °C. **b** Profile of voltage, capacity, T, ΔP, ΔS, and analysis on dP/|dQ| and dS/|dQ| with the C-rates from 0.2 C to 3 C at 25 °C. **c–e** Evolution of **c** T, **d** ΔP, and **e** ΔS at 10-cycle intervals in the 200 cycles for an intelligent pouch cell (1.1 Ah) for charging and discharging at 1 C collected by IISAS under 25 °C. **f** Maximum T, ΔP, and ΔS at 10-cycle intervals in the 200 cycles. **g** Validation on the estimated and practical battery SOH for the intelligent cells. **h** Averaged lowest mean absolute error (MAE) and root-mean-square error (RMSE) for the validation cells with the combination of relevant features.

were recorded when the pouch cell cycled at 1 C (1 C = 155 mA g⁻¹) after formation process. To evaluate the performance of IISAS, thermal and mechanical signals are measured by commercial sensors as well. The T-profile provides an overview on the heat generation and energy transformation, which summarizes reversible entropic heat, irreversible mass transfer, charge transfer, and Ohmic heat. The thermal model is expressed as Eq. (1) in "Method". The state-of-charge (SoC)-dependent entropy and overpotential heat generation that lead to temperature changes associated with the electrochemical process are

essential for the thermal behavior[29]. Besides thermal effect, electrochemical process also induces mechanical changes in the terms of pressure and strain. The extraction of Li⁺ from positive electrode and insertion into negative electrode during charging process leads continues expansion of cell volume, resulting an increasing on the ΔP and ΔS profiles. Since the electrochemical process is highly reversible in current operating protocol, the pressure and strain values return close to their initial level after discharging process. Signals collected by commercial sensors and IISAS remain consistent in trend and

quantified value, indicating high accuracy in feature extraction by IISAS. Their reliability forms a solid foundation for further states self-assessment via intelligent system.

As shown in Fig. 3b, increasing the current rate from 0.2 C to 3 C leads to distinct T-profiles, and elevates the maximum surface temperature of sample cell by roughly 8 °C. Such strong dependence of high current on heat behavior is due to the generation of Joule heating and inefficient thermal conductivity[30]. As higher currents are limited by Li$^+$ diffusion and the aggravated overpotential, a faster and more pronounced heat release can be observed, especially at the end of the discharge stage.

Regarding the changes of mechanical features, ΔP- and ΔS-profiles demonstrate similar trends upon insertion and extraction of Li$^+$ in-between the host structure during the electrochemical process. Although the working mechanisms of both pressure and strain sensor are established on the basis of the expansion and contraction at different electrochemical stages[31,32], the unique structural design of low TCR enables complementary sensing for the reaction-induced expansion and thermal-induced expansion. The pressure sensor focuses on the measurement of force along the radial axis without interference from winkle-type strength. During the charging process, Li$^+$ extraction from positive electrode and insertion into negative electrode would cause a rapid growth of pressure at initial stage and long plateau for the rest of charging period. Variation range of load pressure narrows down as the current rates increase from 0.2 C to 3 C, whereas these reductions are attributed to the proportion of Li$^+$ that participate in the electrochemical process due to kinetic effect. More Li$^+$ are accumulated at negative electrode side with similar level of maximal pressure. The strain sensor measures the deformation degree of packing foil, which closely follows the irregular curved path of the cell body, and commonly varies within the scope of 0.2%[33]. On the contrary, the maximum and minimum values of strain signals in ΔS displays opposite trend as ΔP-profile at the end of charge and discharge process. These differences come as a result of various competing factors, such as the electrochemical reaction dominating the variation and the presence of decomposed gases in the cell. As the current goes above 2 C, the pressure increases at a faster rate, associating with less recoverable range than the lower current rates. Meanwhile, significant increment on the maximal strain value could be observed from the ΔS-profile, which does not follow the previous trend at increasing current due to the thermal expansion of decomposed gases. The fast cycling would result in more complicated status tracking in the battery operating system. $dP/|dQ|$ is believed to serve as an effective descriptor for quantitative analysis on Li-plating, because fast cycling drives Li-plating as a higher pressure change per unit of charge than Li$^+$ intercalation[31]. However, this critical value views the problem from its particular and limited frame of reference, which may change according to the chemical composition and battery operating conditions. The integration of thermal and mechanical sensors reduces the burden on decoupling the representative features and signal crosstalk, enabling a precise and comprehensive analysis for the insights into internal dynamic states.

Herein, the assessment is processed on an integrated model for complex cases, with the comprehensive consideration on electrical, mechanical, and thermal effects. During the rate testing, IISAS provides coordinated analysis on electrochemical process. Li-plating increases internal pressure during fast cycling due to kinetic factor, but this process is also influenced by the thermodynamics because of the induced thermal effect on deposition morphology[34]. Three main peaks could be identified from the initial to end stages in $dP/|dQ|$ profile for either charging or discharging process, whereas the intensity of each peak changes with the current rate. As the current rates increased from 0.2 C to 3 C, the first peak at low voltage in the initial stage of $dP/|dQ|$ profile from each cycle is significantly reduced, leaving the residual last peak at the end of the charging stage. This suggests that Li$^+$ insertion in graphite at the beginning of charging process is strongly limited, whereas the remaining charging peak arises from kinetic-related large overpotential and the issue of Li-plating. Given the fact that Li$^+$ insertion and extraction in host structure should be highly reversible during electrochemical process, the unsymmetric of $dP/|dQ|$ account for the accumulating behavior of Li-plating with thicker SEI layer in each cycle. The top-view and cross-sectional SEM images for the negative electrode of disassembled cell confirm the formation of dendritic-Li at the current rate of 3 C (Supplementary Fig. 26). In order to quantify the irreversible active-Li loss during cycling, the integral charging and discharging area of $dP/|dQ|$ for each cycle is calculated according to Eqs. (3–5) to obtain the corresponding S_2/S_1 ratio (Supplementary Fig. 27), which is highly consistent with the result of Coulombic efficiency in the first cycle of current increases. Less Li$^+$ is extracted from the negative electrode due to the fast kinetic in discharging process, resulting reduced integral area ratio with lower Coulombic efficiency. As the current rate goes back from 3 C to 1 C, the plated-Li and part of residual Li$^+$ in the host are reactivated, that directly lift S_2/S_1 ratio above 100%. It can be concluded that this type of Coulombic inefficiency is mainly related to the kinetic-induced temporary irreversible-Li, which could be released just by reduced current density. Beside the issue of Li-plating, high current induced thermal effect also causes gas volume expansion. The ΔS-profile indicates the electrochemical reaction dominated expansion is transformed to the synergistic process with the contribution of both reaction and thermal expansion at high rates. As a result, it yields unsymmetric pattern from the $dS/|dQ|$ profile, whereas the maximal strain changes only occur at the end of charging with an overlaying effect and the beginning of discharging due to fast cooling during the rest period.

Figure 3c–e demonstrate the evolution of T, ΔP, and ΔS profiles for one sensorized cell over 200 cycles. As shown in Fig. 3c, the T-profiles demonstrate similar trend during the electrochemical process of each cycle, but differences on the pattern could still be observed. This Arrhenius-type behavior can be attributed to heterogeneous internal heat generation and transmission process, whereas reaction gradient and diffusion kinetic are controlled by unevenly distributed SEI layer[35]. Growth of SEI layer and accumulation of side reactions increase the internal resistance, thus resulting in a rising temperature with continuous cycling. Different from the variation on T-profiles, ΔP-profiles are highly consistent (Fig. 3d), especially for the charging region of each cycle. The changes of intensities for each region at different cycles could be assigned to the inhomogeneous electrochemical process with the participation of varied amount of Li$^+$, which commonly appears through the electrode plane. Decomposed gases may raise as the appearance of broad peak or increased peak intensities in twenty cycles (Fig. 3e), which is gradually consumed with the progress of following cycles[36]. The changes on the maximal values in T, ΔP, and ΔS profiles over cycling are quantitatively summarized in Fig. 3f. Accumulation of structural degradation and irreversible side reactions drive capacity fading, while by-products lead to an increased internal resistance and mechanical changes with cycling. The increasing of internal resistance attributes to a thicken SEI layer, which resulting in growth of T_{max}. Continuous increases of ΔP_{max} are identified in 90 cycles, suggesting that part of the active-Li from the positive electrode is consumed to thicken the negative electrode with irreversible Li-loss and dead-Li. Then efficient insertion and extraction of Li-ions are achieved with a highly recoverable pressure changes in the following cycles. The value of ΔS_{max} gradually rise with cycling until 130 cycles, indicating that gas generating rate is reduced and part of gases may be slowly consumed or absorbed inside the cell during cycling. Fluctuation occasionally occurs in these thermal and mechanical profiles, corresponding to the heterogeneous degradation process.

Datasets collected by IISAS have provided substantial insight into the complex dynamic evolution of LIBs. All the sensors demonstrate well-performed durability with precise signal recording for 1180 cycles

(until capacity drops down to 80% of the initial stage), fulfilling the requirement for the service life of LIBs (Supplementary Fig. 28). Besides the contribution to status assessment, the capability of integrated analysis allows an advancement for battery SOH estimation, which overcomes the inherently restriction of electrical datasets. In this work, the term SOH refers to the capacity retention on the ratio between the present and the initial cycle. A data-driven deep-learning framework is developed with the combination of convolutional neural network (CNN) and long short-term memory (LSTM) base models to process the relevant features via machine learning approach for SOH estimation. As illustrated in Supplementary Fig. 29, the framework is established based on two constructive layers, including the primary CNN and the secondary LSTM. The CNN frontend extracts local features; the LSTM backend processes abstracted temporal patterns, reducing computational complexity. The combination of both can achieve the capture of latent features of battery data and efficient prediction. The datasets of lab-assembled intelligent pouch cells were collected for model training, validation, and testing. More about the design ideas of the model and the data processing process are illustrated in the Method. The validation results demonstrate highly accurate capacity estimation by our data-driven machine learning approach, with a lowest mean absolute error (MAE) of 0.5826% and root-mean-square error (RMSE) of 0.8406% (Fig. 3h). The estimated accuracy is significantly improved with combined features on the basis of intelligent model for the realism of the circumstances within the confined dimensions.

Faults diagnosis

Several fault scenarios are simulated to collect response signals and to extract representative features via data-mining. To ensure the electrochemical performance and fidelity of sensor readings, the datasets collection of each channel took place after preliminary test.

Over-charging and over-discharging Over-charging is one of the most common electrical abuses leading to safety accidents. To trigger an overcharge scenario, the cutoff voltage of sample cell is adjusted from 4.2 V to 4.8 V after operating at 1 C for two cycles (Fig. 4a). During the over-charging stage, the electrolyte decomposed at a locally negative overpotential of negative electrode and cause Li-plating[16], decomposing and regeneration of the SEI layer with the consumption of active components in the cell, and sustained gas generation. Hence, obvious changes could also be identified from the temperature, pressure, and strain sensor. Different from the long plateau in T- profile within the voltage of 3.8 V to 4.2 V, temperature continues elevating above 4.2 V, which induces irreversible reactions and drives parasitic reactions to thermal runaway[37]. Expanded pressure variation range and appearance of new peak in dP/|dQ| stand for the occurrence of oversaturating Li-plating during charging in the cell, whereas the fully recoverable pressure and unsymmetric dP/|dQ| profile in discharging process indicate a distinct delithiation behavior from regular process. Dramatical increases in ΔS and its corresponding dS/|dQ| can be assigned to the amount and rate of gases formation from decomposed electrolyte as side reactions, which responsible for unrecoverable cell-bulging. Besides the presence of these apparent features, over-charging also accelerates the phase transformation for the lattice structure of NCM as well, which turns from the layered structure to the disorder rock salt and spinel phases with reduced chemical and thermal stability[38], resulting to a deteriorated resistance against thermal runaway. Apparently, over-charging accelerates battery aging with increased impedance, heat productions, and cell expansion, which induces safety risks for further operation.

Similar to over-charging, cells connected in series could be subject to over-discharging condition as well, the protocol and relevant features are shown in Fig. 4b. The temperature continues to increase after 100% depth of discharge (DOD) at 3.0 V, which is the highest temperature point in the regular end of discharged state. Over-

discharging leads to a rapid voltage drop to −1.12 V (nearly 125% DOD) with a series of irreversible deteriorations, including extraction of remaining Li, decomposition of SEI, and corrosion of Cu current collector into dissolved Cu^{2+}. The growth of peak intensity in ΔS-profile attributed to the generation of gases from decomposed SEI, such as carbon dioxide[39]. The slope in dS/|dQ| indicates that gas generation during over-discharging is much serious than overcharging. The voltage tends to recover as discharging continues, which stabilized at close to 0 V due to the deposition of Cu^{2+} on positive electrode with destroyed porosity. Accumulated Cu-deposition induces decreases in ΔP-profile, and could further result in internal short circuit[40,41].

Li-plating at low temperature. Since Li-plating occurs easily under high current or low temperature conditions during the charging process, here the pouch cell was first cycled at 25 °C and then cooled down to 10 °C to drive Li-plating. As shown in Fig. 4c, obvious changes can be observed from the variation ranges and their corresponding patterns of T, P, S-profiles. Li-ions diffusion in the negative electrode is severely hindered at low temperatures, causing the Li-ions mainly accumulate at the graphitic surface rather than evenly distribute across the negative electrode bulk. The negative electrode surface potential drops to the potential of metallic-Li, offering the conditions for Li-plating at localized regions[42]. The ΔP-V profile shown in Supplementary Fig. 30a demonstrates strong polarization accompanied with most pressure increasing range shifted to the voltage above 4.0 V. The pressure variation range (ΔP) continues narrowing with the formation of irreversible-Li in following cycles, which is consistent with the vanish of peak at 3.75 V and gradually reduced peak intensity at high voltage range in dP/d|Q| profile. Low temperature limited ionic diffusion and lowered reaction kinetics at reduced temperature[34], leading to reduced Li$^+$ insertion and extraction from graphite. Coulombic efficiency in first cycling at 10 °C is significantly depressed, indicating large amount of residual Li$^+$ remains in negative electrode. Besides that, nonuniform current flow at low temperature leads to the growth of dendritic-Li, resulting in the enhanced dP/|dQ| value (above 0.7 MPa/Ah) and suppressed peak area ratio than cell cycled at the temperature of 25 °C Supplementary Fig. 30b). Appearance of dendritic-Li is confirmed by the optical and SEM images of the graphite negative electrode from disassembled cell (Supplementary Fig. 31). Besides the issue of Li-deposition, the contraction of ΔS variation range is caused by the reduced Li$^+$ activity as well. As a result, the comprehensive effect of kinetic and thermodynamic factors drives the battery evolution behaviors at low temperature, and the representative features extracted from the intelligent system are in agreement with the observation in electrochemical performance and morphology characterization.

Internal short circuit. The case of internal short circuit often appears during overcharge when Li dendrite overgrows to the other side. Here, we demonstrate a case that is occasionally occurred during the rest period after discharge process without any external stimulation, which enriches the realistic situation. The sample cell was first operated with the current rate of 1 C for 10 cycles at 25 °C, and then electrochemical performance and response signals of last 3 cycles are demonstrated in Fig. 4d. The preliminary analysis on electrochemical performance during cycling shows a dP/|dQ| value over 1 MPa/Ah and peak ratio higher than 1.0 (calculated via Eq. (11)), suggests a high risk of severe Li-plating already starting in initial cycles. During the rest period, the temperature, pressure, and strain slightly yet continuously increase for 69 min until a sudden drop of voltage, which demonstrate clear evidence of abnormality with regular case shown in Fig. 3a. The cell voltage drops to 0.5 V within 0.1 s and then immediately returns back to previous level. A small peak on ΔP and ΔS-profile appears after the instantaneous change of voltage, while the temperature gradually reduces to ambient temperature. After another 40 min, the sharp
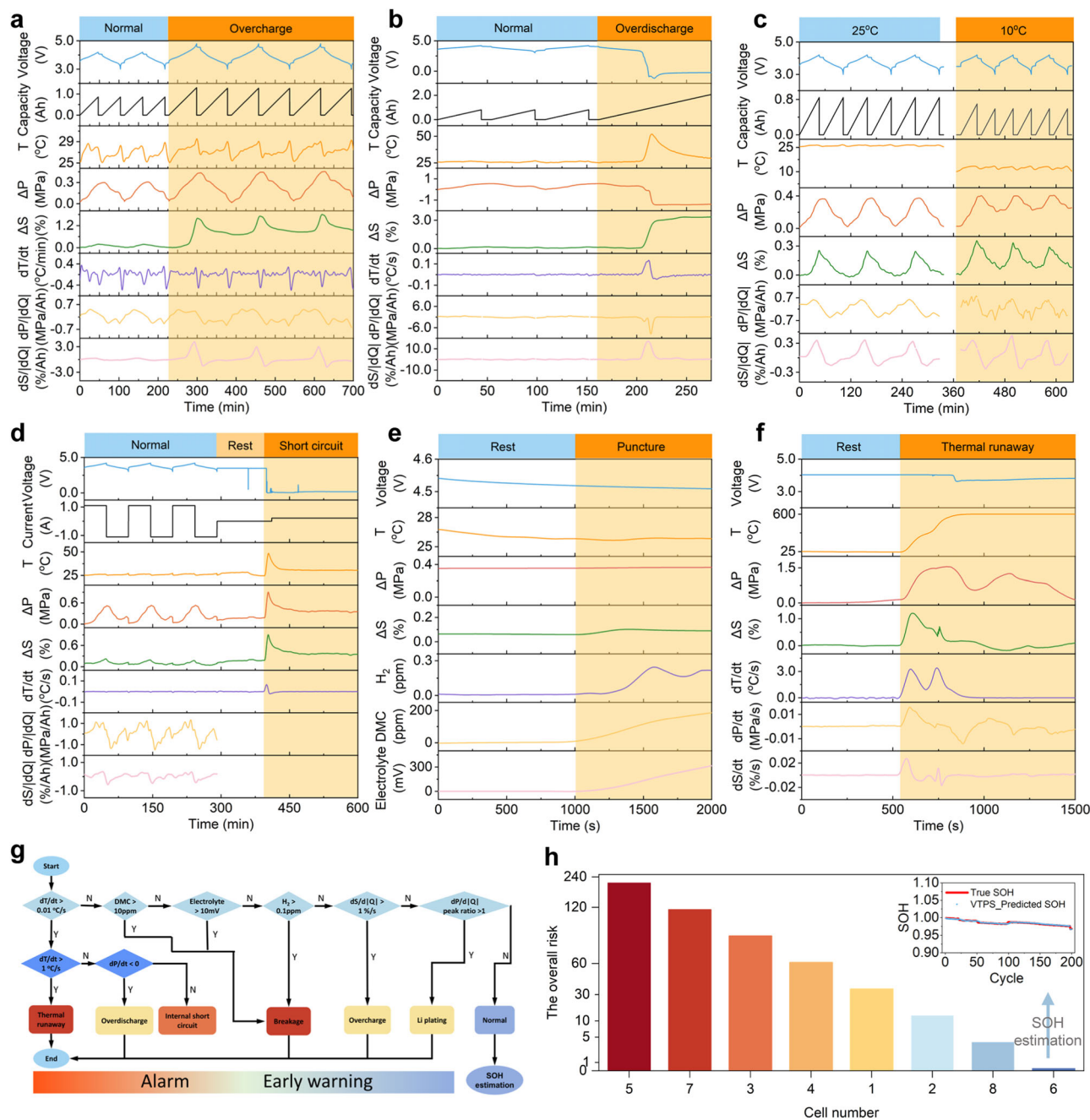
Fig. 4 | Operando monitoring of battery performances under different fault scenarios. a, b Intelligent sample cell operated at different cut-off voltages for **a**, over-charging (4.2 V change to 4.8 V) and **b**, over-discharging (3.0 V change to −3.0 V). **c** Intelligent sample cell cycled under 25 °C and then changed to 10 °C for Li-plating. **d** Occurrence of internal short circuit in intelligent sample cell during rest period. **e** Intelligent sample cell punctured by ceramic knife for mechanical failure. **f** Thermal runaway of an overcharged intelligent sample cell via heating up to 240 °C. **g** Diagnosis workflow for battery-states identification. **h** The comprehensive risk of eight sample cells and SOH estimation on the healthy cell. All the sample cells were cycled at the rate of 1 C.

voltage drop occurs again, and directly goes down to 0.1 V. Notably, the temperature rapidly increases to nearly 48.5 °C, which is much higher at the local internal short circuit point due to heat transmission gradient. As the internal short circuit occurs at a high SoC state, the cell may experience more vigorous heat release, directly leading to thermal runaway. A dramatic drop on the ΔP-profile could be attributed to the melting of residual deposited-Li at the beginning stage[43]. Due to the occurrence of high temperature at the shorted spot, the generation of higher current around this shorted region occurs alongside the faster kinetics. Meanwhile, active materials are depleted faster near the short circuit location to cause further non-uniformities, and then gradually rearranged by the relaxation of the ion distribution[44]. The

internal short circuit also triggers serious electrolyte decomposition and gas generation at high temperature, resulting in a strain behavior of non-electrochemical origin. In the absence of the anomaly on temperature and strain signals collected by IISAS, warning relay on the solid evidence of electrical signal can only be activated after a delayed period. In addition, poor electrical contact may also occur after turbulence, leading to false alarms in fault diagnosis. Therefore, there is a great safety value in the application of early diagnosing internal short circuit and raising the alarm for warning battery state. Besides that, the evolution process could be continuously tracked with the operando monitoring. Insights into the formation mechanism can be identified at the initial stage, allowing for the implementation of control or

prevention strategies before the cell system undergoes irreversible damage.

Mechanical failure by puncture for breakage. Real-time monitoring of mechanical failure induced by puncture was performed using an overcharged sample pouch cell. Usually, the nail penetration test is conducted with a metallic object, and the sharp voltage drop represents solid evidence for the occurrence of penetration. However, penetration may also occur with an electrical insulating object. To capture mechanical failure in more complex scenario, the puncture action is specifically carried out with ceramic insert. Experimental setups for puncture measurement of overcharged pouch cell and movie for the puncture process are shown in Supplementary Fig. 32 and Supplementary Movie 1. Figure 4e displays the response signals of IISAS from the rest stage to the completion of puncture test. Although the ceramic insert has deeply penetrated into the cell body, no abnormal variation can be identified from the voltage profile. It remains at a nearly constant level since the beginning of the rest period. This suggests that reliance on electric signals could lead to inactivated risks identification and delayed warning alarms. Among all the response signals after breakage, the DMC sensor takes the lead in responding detection of gases within 6 s due to the vaporization of DMC from the leaked electrolyte. Meanwhile, part of the leaked electrolyte wets the absorbing layer to activate the potential difference of the electrolyte sensor. Since the immersion process is slower than gaseous diffusion, the response of electrolyte sensor is delayed by seconds after DMC vapor sensor. The H_2 is identified slightly slower than DMC vapor and electrolyte sensor, attributing to the pressure equilibrium process between internal and external of the cell body, which also raise the strain as air infiltrating into cell. Considering the fact that the puncture does not always occur close to the location of the electrolyte leakage sensor, and gaseous diffusion could be influenced by airflow and molecular weight, the combination of gases sensors and electrolyte sensor would provide a more reliable risk check than either individual sensor.

Thermal runaway. Thermal runaway is the most severe and dangerous battery failure[45], which may arise from overcharge, internal short circuit, puncture, or overheating by adjacent cell. Thermal runaway in this work is triggered by a heating plate, and the experimental setups are shown in Supplementary Fig. 33 and the movie for the thermal runaway process is shown Supplementary Movie 2. Such heating process was stopped at 240 °C till cell vented with white smoke. The separator was coated with aluminum oxide (Al_2O_3), which maintains strong thermal stability without melting or shrinking, preventing internal short circuit for further irreversible reactions at high temperature. The functionality of thermal and mechanical sensors started to diverge as temperature continuously increased above 100 °C. As shown in Fig. 4f, the point of inflexion on S- profile comes at 142 °C, when the carboxymethyl cellulose (CMC) in strain and pressure sensors, and PVA in temperature sensor loses structurally bound water molecules[46,47], followed by thermal decomposition of most organic components at higher temperature. Although the IISAS fails to reveal the complete reaction details due to inherent limitations in material thermal stability, their response profiles still provide sufficient information for the evolution process at the early stage of thermal runaway. The extracted relevant feature ΔS, and quantified analysis on dT/dt over 1 °C/s, dP/dt over 0.01 MPa/s, and dS/dt above 0.02%/s within after heating from 25 °C could be solid indicators to confirm the initiation of thermal runaway.

Faults identification and classification procedure. According to the summary on the collected response signals under different fault conditions, IISAS is operating on the basis of distributed artificial intelligent framework, delivers a standard procedure on the analysis of relevant indicators for fault identification and two levels of risk to trigger safety alerts. The logical relationship and boundary conditions are introduced in Method and depicted in Fig. 4g, which mainly rely on the absolute value of relevant features and the correlation on the extracted factors. The issues of over-charging and over-discharging, Li-plating at low temperature or fast-charging conditions can activate early precautions, based on the $V, T, \Delta S$, and ΔP profiles as the typical indicators and the ratio of $dP/|dQ|$ as a critical sign. These issues can further develop into internal short circuit and thermal runaway induced by puncture, which are considered to be the most serious issues that should directly activate urgent alarm warning for emergency. As most of the faults could be resulted from multiple factors, IISAS is developed to clearly present the proportion of contributing issues for each sample cell. The analysis is performed with data-driven approach, whereas a series of representative datasets are processed based on Eqs. (6–10) in "Method" for risk evaluation. To simply quantify the overall risk of each cell for classification, the risk value for the cells introduced in this work are weighted on the basis of Eq. (11) (shown in Fig. 4h). The IISAS offers desirable advantages on real-time states monitoring and assessment, which could be easily connected to cellphone or interactive web page for highly intelligent remote monitoring (Supplementary Fig. 34).

Practical deployment in battery pack

Analysis on battery degradation behavior is more complicated at the level of battery pack that consists of multiple cells connected in series/parallel, where the capacity fading could arise from even higher non-uniformities[48]. Thus, it is challenging to identify the failure mechanism precisely. Here, the aging of each cell is evaluated on the basis of data-mining and features analysis. The pack test was conducted with three pouch cells connected in parallel (Fig. 5a, b), and the IISAS provides details on the distinct thermal and mechanical behaviors of each individual cell simultaneously. The electrochemical performance of battery pack is shown in Fig. 5c. The temperature differences are confirmed by infrared (IR) camera (Fig. 5d), it can be clearly observed that the edge-surface of middle cell is 0.8 °C and 0.4 °C higher than the cell located at top and bottom in the term of maximal discharging temperature, respectively. However, the thermal sensor suggests that temperature for the upper-surface of cell-2 is higher than the neighboring ones by 2 °C, as shown in Fig. 5e. The difference on the thermal effect between top and bottom cells is mainly attributed to the distinct degradation behaviors of corresponding cell, which determines internal resistance and current flow. Cell 2 reaches the highest temperature in battery pack due to the contribution of its internal heat generation and overlayed heat transmission from the neighboring cells. Different from thermal behaviors, the variation range and pattern of ΔP and ΔS profiles demonstrate inhomogeneous mechanical properties of individual cells. Cell 1 located at the top of package has a continues narrowed variation range on ΔP profile, which could relate to a faster capacity fading during cycling. Cell 2 demonstrates a more stable variation range and consistent pattern on ΔS profile compared to neighboring cells. Both cells located close to the fixture show a narrowed changes on strain profile, which may relate to the transmission of pressure through the battery pack. Therefore, IISAS reveals a strong correlation between cell location and the terms of mechanical and thermal features. The collected dataset provides comprehensive information for assessment on the degradation behaviors of each cell.

In the actual operation of a battery pack, overcharging/over-discharging often occur due to the dynamic imbalance caused by variations in the aging degree and internal resistance of series-connected battery cells. A battery pack consisting of three series-connected cells was prepared and performed 1 C charge-discharge cycles at 25 °C, with monitoring conducted by IISAS. As observed in Fig. 5f, during the first three cycles, the maximum of ΔP and $dp/|dQ|$ in cell2 were higher compared to the other two cells, while the highest
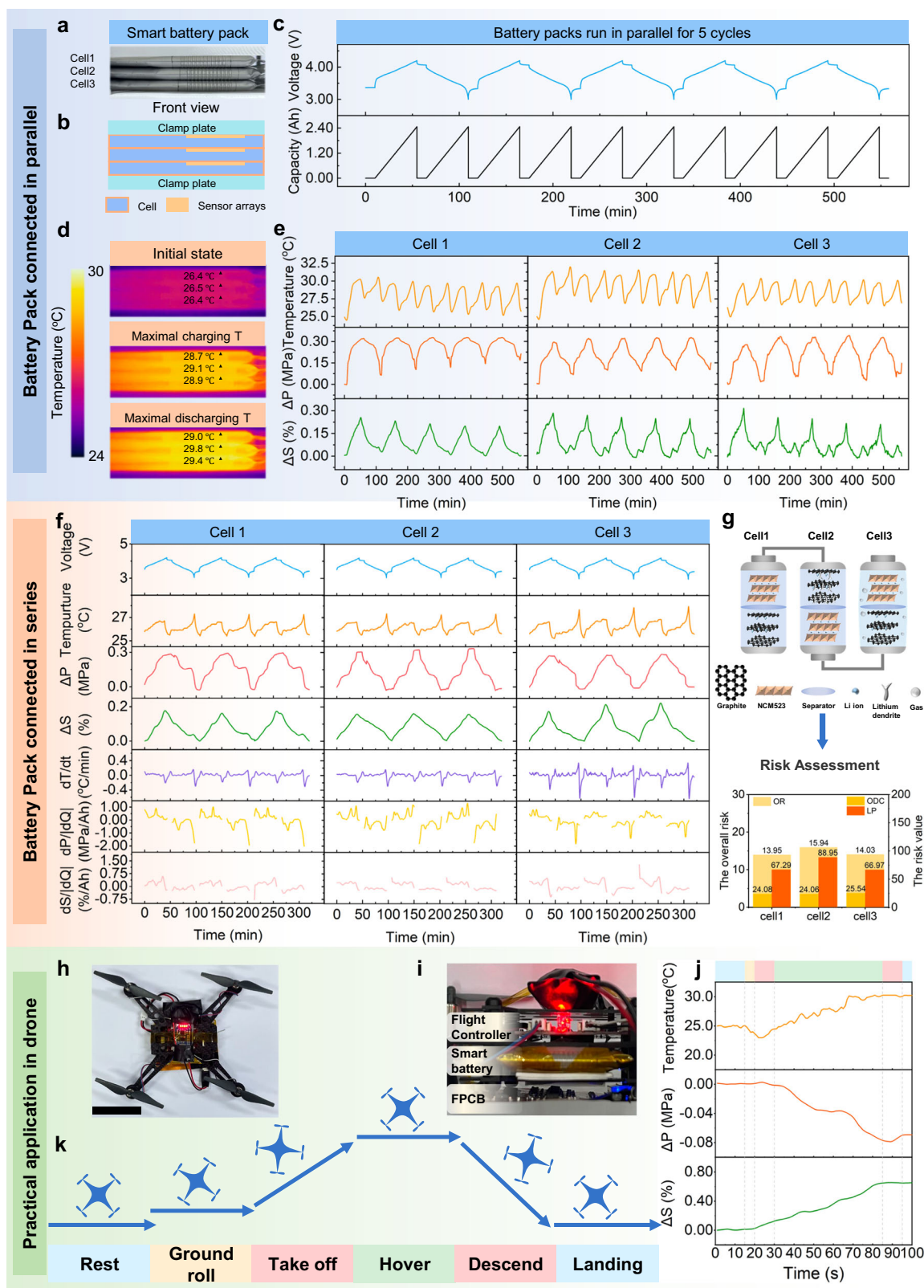
Fig. 5 | Intelligent battery pack with real-time status tracking and practical demonstration with a drone. a Photographs, **b** schematic illustration of pack level intelligent pouch cells. **c** Electrochemical performance of the smart battery pack and **d** corresponding IR images at different states. **e** Temperature, pressure, and strain performance of each intelligent cell during the electrochemical process. **f** Operando monitoring data of each battery performance under the battery pack connected in series. **g** The risk value results of state assessment for each battery in a series battery pack. **h** Photograph of intelligent pouch cell powered quadrotor. Scale bar, 5 cm. **i** Photograph of intelligent cell power system integrated with flight controller of quadrotor. (Circuit board is printed on a flexible polyimide foil (FPCB) to reduce the load). **j** Performance of intelligent cell powered quadrotor at rest, ground roll, take off, hover, descend, and landing period. **k** The flight process of the drone.

discharge temperature and the maximum ΔS of cell3 were also higher. The results from the multi-parameter coupling risk assessment model show that cell2 has a higher Lithium-Plating (LP) risk value, while cell3 has a slightly higher Over-discharge (ODC) risk value (Fig. 5g). However, the difference in the comprehensive risk values is small, indicating a slight electrochemical behavior heterogeneity in the early stage of the battery pack. It is noteworthy that during the 21st to 30th cycle (Supplementary Fig. 35), the maximum of ΔP in cell2 gradually increased, and the highest discharge temperature of cell3 had already risen by 1.5 °C compared to the other two cells. At this point, the LP risk value of cell2 increased by approximately 31%, and the ODC risk value of cell3 increased by about 3.5%. The difference in the comprehensive risk values among the three cells became larger, further exacerbating the imbalance in the battery pack. This dynamic asymmetric degradation phenomenon reveals the strengthening mechanism of the "weakest link effect" in series-connected battery packs. Without implementing active balancing control, the differences between cells will exponentially increase with cycling, ultimately causing a reduction in the battery pack's life. The experimental data confirm that this sensor system can capture the gradient distribution characteristics of the internal state parameters of the battery pack in real-time, providing solid inputs for the differentiated control strategy of the BMS.

Practical application in drone. As a proof-of-concept for practical application, IISAS and LIBs were further integrated with flight controller system to power a quadrotor drone (Fig. 5f, g). The relevant features of battery performances during the ground roll, taking off, hover, descend, and landing periods were recorded (Fig. 5h and Supplementary Movie 3) and transmitted for on-site analysis. The real-time battery states information and suggestions for energy utilization can be processed by board computer. To power four engine propellers, a current flow of 10.7 A with a minimum voltage of 3.7 V is required, equivalent to a rate of 9.7 C for the sample cell. The delivered discharge capacity under such a high current rate is significantly reduced by kinetic effect, thus lower the recoverable range on ΔP-profile with limited Li^+ extraction from negative electrode back to positive electrode. The ΔS-profile demonstrates distinct stress pattern at low current rates with the contribution of combined effects, while thermal expansion at such power density is much stronger than the reversible electrochemical process dominated stress regression. Apart from the contribution of electrochemical reaction, the thermal behavior of battery in practical application also relates to the flow of wind, which leads to fluctuations on the T-profile. The initial drop of temperature at ground rolling and taking off periods can be attributed to the cooling effect of airstream by propellers. The temperature then rapidly increases until flight reaches to descending and landing with less energy consumption.

The IISAS effectively and precisely measured relevant feature changes in battery package and for practical application. These results demonstrate the advantages of IISAS in monitoring and evaluating the state of each individual cell with distinct degradation process, locating distribution, and application fields. Thus, it could provide reliable suggestions for battery operation and energy utilization through intelligent management systems.

Discussion
The urgent demand for the safe operation of LIBs across wide application scenarios requires intelligent system that can ensure precise states assessment and reliable estimation. The embedded conformal sensing arrays in packing foil developed in this work imposes a close to non-detectable burden on energy density and cycling stability. Each sensor delivers high accuracy with rapid response, long-term durability for entire life-cycles, and strong anti-interference against the mechanical/thermal/chemical changes. The developed IISAS establishes a bridge between accumulated nano-scale fundamental evolution and representative features, allowing for precise routine SOH estimation, and enabling reliable and comprehensive tracking of various faults, which are critical for batteries operation during their entire service life. Besides efficient assessment for routine duty and early warning, the dynamic evolution of cell chemistry as well as their corresponding mechanisms are clearly revealed as well. More importantly, the IISAS demonstrates its capability for practical deployment for battery packs in diversified format, chemistry, and engineering fields. This rarely reported onsite sensing system would render next generation batteries intrinsically intelligent.

Methods
Materials
Silver paste (solid content = 50 ± 5%) was purchased from Shenzhen Xinwei electronic materials Scientific Co., Ltd. Aluminum-plastic film was obtain from Shenzhen Xinlun Technology Co., Ltd. Ferric (III) chloride ($FeCl_3$,98%) lithium tetrafluoroborate ($LiBF_4$,99.9%) 3-hydroxytyramine hydrochloride (99%), and palladium (II) chloride ($PdCl_2$,99%) were obtained from Adamas-beta. Dimethyl Carbonate (DMC, AR), hydrochloric acid (HCl,37 wt.%), poly (Vinyl Alcohol) (PVA, AR), isopropyl alcohol, nickel(II) acetate tetrahydrate ($C_2H_6O_4Ni\cdot4H_2O$, AR), and ethanol (AR) were purchased from Chengdu Kelong Chemical Reagent Co., Ltd. (Chengdu, China). Tin (IV) chloride pentahydrate ($SnCl_4\cdot5H_2O$, AR), molybdenum disulfide (MoS_2, AR) nafion perfluorinated resin solution(20 wt.% in mixture of lower aliphatic alcohols and water, contains 34 wt.% water) and 1,2,4,5-tetracyanobenzene ($C_{10}H_2N_4$,97%) were purchased from Shanghai Macklin Biochemical Technology Co., Ltd. 1 M $LiPF_6$ in ethylene carbonate/diethyl carbonate (EC/DEC) electrolyte, lithium bis(fluorosulfonyl)imide (LiFSI, 99.9%), lithium bis(trifluoromethylsulfonyl, 99.9%)imide were provided by DodoChem. Potassium Chloride (KCl, AR) and ammonia hydroxide (NH_4OH) solution (25–28 wt.%) were provided by GENERAL-REAGENT. Poly(3,4-ethylenedioxythiophene): poly(styrenesulfonate) (PEDOT: PSS) solution (1.5 wt.% in water) was obtained from Shanghai Meryer Chemical Technology Co., Ltd. MXene (Ti_3C_2,10 mg ml^{-1}) dispersion was obtained from Jilin Yiyi technology Co., Ltd. Acetone (AR) was purchased from Chengdu Chron Chemical Co., Ltd. Hydrazine hydrate (80 wt.%) was purchased from Chengdu Jinshan Chemical Reagent Co., Ltd. RGO Graphene (98%) was provided by Suzhou-Tanfeng graphene Technology Co., Ltd. Polyvinylidene fluoride (PVdF, AR) and Carboxymethyl cellulose (CMC, AR) were obtained from Zhengzhou Jinghong New energy Technology Co., Ltd. Polyurethane (PU) film was purchased from Shanghai Peijie Medical Equipment Co., Ltd. Polytetrafluoroethylene film (PTFE, AR) was purchased from Yiyuantai Electronic Technology Co., Ltd. Polyethylene glycol terephthalate (PET) film was purchased from Dongguan Baosheng engineering plastic material Co., Ltd. Polydimethylsiloxane(PDMS) precursor (SYLGARD 184, curing ratio 10:1) was purchased from Dow Inc. Multi-walled carbon nanotube for DMC sensor ink (MWCNT, pipe diameter: 3–15 nm, pipe length: 15–30 μm, 99%) was obtained from Shenzhen Huiheng Scientific Co., Ltd. Multi-walled carbon nanotube for pressure and strain sensor ink (MWCNT, pipe diameter: 4–6 nm, pipe length: 10–20 μm, 99%) was obtained from Jiangsu Xianfeng nanomaterials Technology Co., Ltd. Commercial thermistor (XH-T110) was purchased from Hongxinweiye Technology Co., Ltd. Commercial pressure sensors (FSR406) and strain gauges (BF350-3AA) were supplied by Shenzhen Xinglin Hunter Electronics Co., Ltd.

Preparation of sensors ink and patches
Temperature sensor ink: The purchased MXene dispersion was ultra-sonic centrifuged to obtain MXene low-layer/single-layer dispersion, and then the dispersion was lyophilized to obtain MXene nanosheets. The temperature sensor ink was prepared by dispersing MXene nanosheets (1.2 wt.%), PEDOT: PSS solution (16.21 wt.%), PVA (6 wt.%), and isopropyl alcohol (7.5 wt.%) into the aqueous solution.

Pressure and strain sensor ink: CMC was dispersed into a mixture of ethanol, isopropyl alcohol, water, and ammonia (v/v/v/v = 8:2:10:1) to obtain a CMC solution of 4.76 mg/mL. Then 2 mg/mL of dopamine hydrochloride was added and stirred to polymerize the dopamine hydrochloride. Then 0.5 wt.% carbon nanotubes and 0.25 wt.% graphene were violently stirred and ultrasonically disperse.

The PDMS was mixed evenly at the curing ratio of 10:1, then put into the dispensing needle. The 2×2 cm PDMS network microstructure was printed by the micro-electronic printer (Scientific 3, Shanghai Mifang Electronic Technology) on the PET surface, and cured at 90 °C for 2 h. The PDMS film was cleaned by plasma cleaning machine (CSCPIAS, Shanghai Zhongbin Technology). Subsequently, 100 μL of CNT/CB ink was dropped and dried. Finally, The PET film with PDMS network microstructure was cut to a suitable size by laser to obtain pressure sensor patches (Supplementary Fig. 10).

The PDMS was mixed evenly at the curing ratio of 10:1, and then coated into a 300 μm film and cured at 90 °C for 2 h. Then, 25 μL CNT/CB ink was dropped and dried after being cleaned by plasma cleaning machine. The strain sensor patches were obtained after being pre-stretched (5 times) (Supplementary Fig. 13).

Hydrogen sensor ink: The same volume of concentrated ammonia water was added into 30 mg/mL $SnCl_4 \cdot 5H_2O$ aqueous solution. Then the mixture was transferred to a teflon-lined stainless steel autoclave and heated at 120 °C for 12 h. $PdCl_2$ (1 mg/mL) and MoS_2 (0.013 mg/mL) were added to ultrasonic dispersion uniformly, and 10 vol.% hydrazine hydrate was added and stirred for 12 h with reheating. After cooling, the product was centrifuged, the precipitate was thoroughly washed with deionized water and dried under vacuum at 60 °C. The resulting sample was prepared as a 20 mg/mL aqueous solution.

DMC vapor sensor ink: Nickel acetate tetrahydrate (0.86 mg/mL), 1,2,4,5-tetracyanobenzene (2.57 mg/mL), MWCNT (0.14 mg/mL) were ultrasonically dispersed into ethanol solution. Subsequently, the mixture was transferred to a teflon-lined stainless steel autoclave and heated. The sample (NiPPc/MWCNT) was respectively washed with the hydrogen chloride solution and hot ethanol for several times. NiPPc/MWCNT composite was collected by filtration and dried in vacuum at 60 °C for 12 h. Then the dried sample was dissolved in a mixture of ethanol, water, and 0.5 wt% Nafion (v/v/v = 4:15:1) and prepared into NiPPc/MWCNT ink. 1.7 mg of NiPPc/MWCNT were separately dispersed into 3 mL of ethanol to measure ultraviolet–visible absorption spectra.

Preparation of sensor arrays

The fabrication process of the fully printed multifunctional sensor arrays in Al-polymer packing foil substrate is detailed in Supplementary Fig. 1a. Briefly, the surface of the aluminum (Al)−polymer packing foil was etched with grooves to a depth of 20 μm through the laser (MC-E-B, Guangdong Yueming). The grooves were cleaned and polished with anhydrous ethanol, followed plasma cleaning machine (CSCPIAS, Shanghai Zhongbin Technology) and UV-light (UZ205-MC, Shanghai Zhongbin Technology) treatment to enhance the surface wettability. All the sensors are constructed on the basis of Ag circuits and lab-prepared sensitive ink layer. The conductive electrodes for temperature, pressure, and gases sensors consist of interdigitated finger pattern with width of 300 μm and spacing of 250 μm. The Ag circuit of the sensor array was printed in the groove by screen printing machine (ZB3040H, Zhejiang Huaqizhengbang). The Ag/AgCl electrode for electrolyte leakage sensor was obtained by injecting 5 μL 1 M $FeCl_3$ solution on top of one Ag reference electrode using a micropipette[49]. The sensitive layer of the temperature and gases sensors were printed into the patterned electrode grooves via drop-coating 25 μL of prepared ink, respectively. These inks were dried at 80 °C. After that, the strain patch was attached to the circuit of the strain sensor with glue and conductive silver. The pressure patch was applied to the corresponding location with capton. Finally, different membrane materials were used for encapsulation. 10 μL 25 mg/mL

PVdF acetone solution was absorbed by a micropipette and evenly coated onto the surface of the electrolyte leak sensor. PTFE film was encapsulated onto the surface of the gas sensors. PU film was attached as the top encapsulation layer onto the surface of the remaining sensor array to ensure the sustainable operation of sensors against deterioration, oxidation, and moisture immersion.

Process of drop coating

The sensor-sensitive layer ink underwent 30-min ultrasonic homogenization to achieve uniform dispersion without particle agglomeration. Plasma-treated aluminum-plastic film was then mounted on quartz substrates using vacuum fixturing. Deposition was accomplished via micropipette dispensing with controlled flow velocity to ensure electrode uniformity. Subsequent thermal curing at 80 °C for 30 min facilitated solvent evaporation and film consolidation.

Signal conditioning, processing, and wireless transmission circuit design

The circuit diagram of the analog signal conditioning module of IISAS is illustrated in Supplementary Fig. 4b. ESP32-WROOM-32 (Espressif) was utilized as MCU at the core of PCB. By exploiting the MCU's built-in 12-bit ADC block as well as its computational abilities, and wireless serial communication capabilities, the microcontroller conditioned sensor signals through the analog circuit before wirelessly transmitting them to the receiving terminal. Transduction paths for each sensor in the sensing array were processed according to their corresponding sensing mode. The signal of temperature, pressure, strain, and H_2 gas and DMC vapor sensor rely on the chrono amperometry of resistance response. The resistance of these sensors was measured by dividing the voltage with suitable resistor at 1.0 V. The electrolyte leakage sensor measures the voltage differences between Ag and AgCl electrode, which could be activated by the electrolyte. The voltage values of all sensor are transmitted to a low-power AD8226 instrument amplifier for amplification. All the analogue signal conditioning paths concluded with a RC low pass filter aimed at attenuating noise and interference during measurement before transmitting to the MCU. The dataset from the sensor array was collected once per second.

Model for SOH estimation

The design of the CNN-LSTM hybrid architecture is based on the multi-scale spatio-temporal characteristics of battery data: To address the local correlations of sensor signals (voltage, current, temperature, pressure, strain, etc.) along the temporal axis, the 1D-CNN automatically captures such spatial patterns through convolutional kernels, avoiding the subjectivity of traditional manual feature engineering and the high redundancy of fully connected networks. Meanwhile, the degradation of battery health status inherently stems from the long-term cumulative effects of physicochemical processes (e.g., SEI layer growth, lithium dendrite deposition) over hundreds to thousands of cycles. The LSTM effectively models these long-range dependencies through its gating mechanisms, overcoming the limitations of standalone CNN or RNN in temporal modeling. The hierarchical structure—utilizing the frontend 1D-CNN for local feature extraction and the backend LSTM for global degradation pattern analysis—reduces high-dimensional data processing complexity while deeply mining latent spatio-temporal correlation features in battery data. We conducted additional analysis on the same dataset separately using the individual CNN model and the individual LSTM model. As shown in Supplementary Fig. 36a, b, the prediction accuracy of the CNN-LSTM hybrid model is higher than that of the individual models, further demonstrating the superiority of the hybrid architecture.

Data preprocessing: Firstly, the original data flow, including battery voltage (V), temperature (T), pressure (P), strain (S) in each battery cycle is averaged to obtain the feature (V_{Mean}, T_{Mean}, P_{Mean}, S_{Mean}). This calculation of the mean value can suppress the instantaneous noise

during the charging and discharging process. Then, the characteristic values are normalized according to X' = (X-X_initial)/X_initial, so as to reduce the individual differences of the battery.

The sensor data and electrochemical data of the smart battery were inputted in the format of (batch-size = 8, L = 10, input data's feature dimensions + 1). These data were processed through one-dimensional CNN to obtain input features for the LSTM. The one-dimensional convolutional parameters are as follows: input-size = input data's feature dimensions, out_channels = 1, kernel = (1, 1). The resulting output was subsequently normalized via batch normalization and activated using the sigmoid function. Then the processed data was used as features input into the LSTM, with LSTM parameters set as input-size = 1, hidden-size = 128, and num_layer = 3. The LSTM's output was passed through a fully connected layer, with parameters in-features = 128 and out-features = 1. Besides, these optimal parameters of the model are determined through grid search, where a set of discrete values is assigned to each hyperparameter, forming a grid of hyperparameter combinations. The experimental results are shown in Supplementary Fig. 36c–k. By traversing all possible hyperparameter combinations and using cross-validation to evaluate the model's performance for each combination, the combination with the bettter performance is ultimately selected as the model's hyperparameters. The results show that when the number of layers (nl) = 3, layer sizes (hs) = 512, batch sizes (bs) = 8, training set sizes = [1,2,3], training losses versus the number of epochs (ep) = 60, the error is minimized and the prediction effect is optimal.

Thermal model

The inevitable thermal model can be expressed as follows:

$$Q = I(V - U) + IT\frac{\partial U}{\partial T} - \sum_i \triangle H_i^{avg} r_i - \int \sum_j (\bar{H}_j - \bar{H}_j^{avg})\frac{\partial c_j}{\partial t} dv \quad (1)$$

whereas I refers to the operating current and V stands for the operating voltage, U represents the open voltage, T means ambient temperature, and $\frac{\partial U}{\partial T}$ accounts for the voltage temperature coefficient[29,50]

Irreversible Li-loss

The quantification of irreversible Li-loss at each cycle is calculated based on the ratio of integral area between discharging and charging process, which derive formulas according to the Chain Rule:

$$\int \frac{dP}{|dQ|} dt = \int \frac{dP}{dt}\frac{dt}{|dQ|} dt = \int \frac{\frac{dP}{dt}}{C} dt = \frac{P(t)}{C} \quad (2)$$

$$S_1 = \int_{t_1}^{t_2} \frac{dP}{|dQ|} dt = \frac{P(t_2) - P(t_1)}{C} \quad (3)$$

$$S_2 = \int_{t_2}^{t_3} \frac{dP}{|dQ|} dt = \frac{P(t_3) - P(t_2)}{C} \quad (4)$$

$$\frac{S_2}{S_1} = \frac{P(t_3) - P(t_2)}{P(t_2) - P(t_1)} \quad (5)$$

whereas P stands for pressure; Q refers the capacity; C is the constant current at current charge and discharge process; t represents the time; $P(t)$ is a function of pressure change over time, $P(t_1)$ is the pressure at the beginning of charging, $P(t_2)$ is the pressure at the end of charging, $P(t_3)$ is the pressure at the end of discharging.

S_1 is the integral area of $dP/|dQ|$ integration over t in the charging stage, S_2 is the integral area of $dP/|dQ|$ integration over t in the discharge stage.

$P(t_3) - P(t_2)$ is the pressure difference between the end point and the beginning point of the discharge stage. The bulk shrinkage of graphite is mainly caused by the removal of Li-ions.

$P(t_2) - P(t_1)$ is the pressure difference between the end point and the beginning point of the charging phase. The bulk expansion of graphite is mainly caused by the insertion of Li-ions and the formation of Li-dendrites.

$\frac{S_2}{S_1} = 1$, shows that the charge-discharge process is completely reversible.

$\frac{S_2}{S_1} < 1$, means that the amount of Li-ions removed from negative electrode is less than the amount of Li-dendrites embedded and formed, which may relate to the formation of Dead-Li.

$\frac{S_2}{S_1} > 1$, represents more Li-ion released or reactive from negative electrode, or even the regression of Li-dendrite.

Fault risk assessment calculated as follows:

Thermal runaway risk value (TR):

$$TR = \frac{T_{max}}{27.5} + \frac{\frac{dT}{dt}_{max}}{0.003} \quad (6)$$

Breakage risk value (P): if H_2/DMC/ Electrolyte leakage >0, P = 100; if H_2/DMC/ Electrolyte leakage = 0, P = 0

Internal short circuit risk value (ISC):

$$ISC = \frac{T_{max}}{27.5} + \frac{\triangle P_{max}}{0.25} + \frac{1}{V_{min}} \quad (7)$$

Overcharge risk value (OC):

$$OC = \frac{\triangle P_{max}}{0.25} + \frac{\triangle S_{max}}{0.28} + (V_{max} - 4.3) \times 20 \quad (8)$$

Over-discharge risk value (ODC):

$$ODC = \frac{\triangle P_{min}}{-0.25} + \frac{\triangle S_{max}}{0.28} + (2.8 - V_{min}) \times 20 \quad (9)$$

Li-plating risk value (LP):

$$LP = \frac{\triangle P_{max}}{0.25} + \frac{\frac{dP}{|dQ|}_{Peak3\ max}}{\frac{dP}{|dQ|}_{Peak2\ max}} \times 10 \quad (10)$$

whereas representative value for $T_{max}, \frac{dT}{dt}_{max}, \triangle P_{max}, \triangle S_{max}, V_{max}, V_{min}$ is obtained from the statistical results of sample cells on the standard operating procedure.

$$\frac{dP}{|dQ|} \text{ peak ratio} = \frac{\frac{dP}{|dQ|}_{Peak3\ max}}{\frac{dP}{|dQ|}_{Peak2\ max}} \quad (11)$$

$\frac{dP}{|dQ|}_{Peak2max}$ is the second peak value of the $\frac{dP}{|dQ|}$ curve.

$\frac{dP}{|dQ|}_{Peak3max}$ is the third peak value of the $\frac{dP}{|dQ|}$ curve.
The overall risk (OR):

$$OR = TR \times 200\% + P \times 100\% + ISC \times 50\% + OC \times 30\% + ODC \times 30\% + LP \times 10\% \quad (12)$$

Preparation and test of pouch cells

The commercialized rolled graphite ||NMC532 cell body (nominal capacity of 1100 mAh) with Al_2O_3 coated polyethylene (PE) based separator (Dry Cell Assembly (DT424057-1100) was purchased from Dongguan Data Power Co., Ltd. Separator detail: thickness 12 μm, porosity 47–50%, lateral size 52 mm.) were packed by integrated

sensing arrays packing foil, and filling with 3 ml electrolyte (1 M LiPF$_6$ in EC/DMC with weight percent ratio 1:1) in glovebox under argon atmosphere. The pouch cells were sealed at −93 kPa, 180 °C for 3 s. Then the pins of sensor array were connected to lab-designed PCB via lab-prepared soft wire circuit (Supplementary Fig. 1g). And the sample cells were applied with around 0.2 MPa contact pressure through the screw fixing fixture. Cycling tests were conducted in the voltage range between 3.0 and 4.2 V with rest period of 10 min by CT-4008Tn-5V6A Battery Test System (Neware Technology Ltd., China) in a temperature-controlled chamber at 25 °C (LC-MJX-70BE, accuracy: ±1 °C).

The characterization of the sensors

Individual performance tests for each sensor were performed by the Electrochemical Workstation Analyzer (VIONIC, Metrohm Autolab). The on-battery test data of the sensor array is collected by the designed PCB. All the sensors displayed well-performed durability along the entire service lifetime. The temperature, pressure, and strain sensor work associating with repeatedly cell volume changes. Although the sensors for H$_2$ gas and DMC vapor still maintains high accuracy on gas detection and are capable to be reused, the activation of gas sensors is same result as electrolyte leakage sensor. The failure cell needs to be replaced with intergrade sensor array.

Calibration of hydrogen sensor

The Calibration model of hydrogen sensor is expressed as follows:

$$\Delta C = \left(\frac{R - \partial_T \partial_S R_0}{\partial_T \partial_S R_0 \beta_T \beta_S S_0} \right)^2 \tag{13}$$

Whereas ΔC refers to the hydrogen detection concentration and R refers to the real-time resistance of the hydrogen sensor. R_0 refers to the reference resistance of the hydrogen sensor (20 °C, strain = 0%). S_0 refers to the reference sensitivity of the hydrogen sensor (20 °C, strain = 0%). ∂_T means temperature reference resistance coefficient, and ∂_S means strain reference resistance coefficient. β_T means temperature reference sensitivity coefficient (20 °C, strain = 0%), and β_T means strain reference sensitivity coefficient (20 °C, strain = 0%).

The sensitivity of the hydrogen sensor is defined as:

$$S = \frac{\Delta R}{R_0 \Delta C^{0.5}} \tag{14}$$

The variation of the baseline resistance of the hydrogen sensor at different temperatures (20–60 °C, 0%). The temperature calibration model is obtained (Supplementary Fig. 37a, b). The temperature compensation model is:

$$R_T = -2.784T + 333.76 \tag{15}$$

$$S_T = 0.0009T^2 - 0.0162T + 4.72 \tag{16}$$

$$\partial_T = \frac{R_T}{R_0} \tag{17}$$

$$\beta_T = \frac{S_T}{S_0} \tag{18}$$

The variation of the baseline resistance of the hydrogen sensor at different strains (0–8%, 20 °C). The strain calibration model is obtained (Supplementary Fig. 37c, d). The strain compensation model is:

$$R_S = -2.775S + 278.02 \tag{19}$$

$$S_S = -0.01612S^2 - 0.0804S + 4.8154 \tag{20}$$

$$\partial_S = \frac{R_S}{R_0} \tag{21}$$

$$\beta_S = \frac{S_S}{S_0} \tag{22}$$

Validation: The model was verified based on the data collected from the uncalibrated points, and the verification showed that the calibration error of the model was less than 5% (Supplementary Fig. 37e–h).

The setup for cells operating under different scenarios

The fixture of the designed soft-pack battery was purchased from Shenzhen Jialichuang Technology Group Co., Ltd. (Supplementary Fig. 1f) according to the size of cell. All the sample cells were applied with around 0.2 MPa contact pressure through the screw fixing fixture, and operated in a temperature-controlled chamber at 25 °C (LC-MJX-70BE, accuracy: ±1 °C) for formation cycles and preliminary tests. Four windows were opened in the fixture for gas sensors, electrolyte leakage sensor, and the strain sensor, which facilitate to perform their functionalities.

The setup for cells operating in pack

The fixture for cell-pack was also lab-printed without open window. Three pouch cells were paralleled connected in pack, and closely overlayed under 0.2 MPa pressure without any thermal conductive medium. Cycling of pack was conducted in the voltage range between 3.0 and 4.2 V with rest period of 10 min by CT-4008Tn-5V6A Battery Test System (Neware Technology Ltd., China) in a temperature-controlled chamber at 25 °C (LC-MJX-70BE, accuracy: ±1 °C).

Application demo

Drone model 8523 used in this work as intelligent cell powered quadrotor with rated voltage of 3.7 V and rated power of 9 W, that was purchased from Xinyouduo Ltd., China. The load speed and load current of each engine is 25750 rpm and 2.678 A, respectively. The substrate of PCB was changed to flexible PI foil as FPCB to reduce the load, and the IISAS is intergraded with flight controller system for on-site data collection and analysis.

Data processing

The analog signals output by the microcontroller are used to calculate the resistance values of the sensors based on the principles of voltage division and the settings of the amplification circuits. These resistance values are then utilized to determine the changes in the actual physical quantities, considering the linear relationship between the measured physical quantities of each sensor and the resistance change rate. For long-term battery testing data, the temperature sensor signals need to be adjusted by setting the baseline to the ambient temperature at the start of each cycle to correct for drift over time. For pressure and strain sensor data, baseline calibration is achieved by just adjusting the intercept so that the value at the start of the first cycle is zero.

Materials characterization

The morphologies and chemical distribution of each sensor were studied with GeminiSEM 300 (ZEISS, Germany) for the top-view and cross-section image and EDS mapping. The cross-section image of sample was collected by freeze cutting process. Samples were immersed into liquid nitrogen for 1 min and then directly took out for cutting. XRD spectra of sensing materials were obtained using

DX-2800 X-ray powder diffractometer (Dandong Haoyuan Instrument Co., Ltd, China). The data were collected from 0° to 50° with a scanning rate of 10° min^{-1}. The X-ray absorption near edge structure (XANES) and Extended X-ray absorption fine structure (EXAFS) spectra of the Ni K-edge were carried out using laboratory X-ray absorption spectrometer (Anhui Absorption Spectroscopy Analysis Instrument Co., Ltd, China.) in the transmission mode, and Si (551) spherically bent crystal analyzers with a radius of curvature of 500 mm was used to acquire the spectra. The XANES and EXAFS data were processed by the Athena and Artemis software package. FTIR spectra was conducted by an infrared spectrometer (Nicolet iS50, America) with a scanning range from 2500 cm^{-1} to 500 cm^{-1}. Raman spectroscopy was tested by Raman Microscope (Thermo Fisher Scientific) with a 455 nm laser source. Ultraviolet–visible absorption spectroscopy was measured using UV–visible spectroscopy (UV–vis, UV1500PC). Thermal image of the surface of the smart battery and the side of the battery pack were investigated with an infrared thermal imager (Fotric, China).

The characterization of the electrodes

After testing at different scenarios, the pouch cells were disassembled in a glovebox under argon atmosphere. The electrodes were washed with DMC solvent to remove residual Li-salts, then dried in vacuum for SEM/EDS (ZEISS GeminiSEM 300) characterization. Cross-sectional image is collected following same preparation process as sensors.

Data availability

The data that support the findings of this study are available within the paper and its Supplementary Information and all data are also available from the corresponding authors upon request. Source data are provided in this paper. Source data are provided with this paper.

Code availability

Code for data processing is available at https://github.com/Hellow-Wor/SOH-projections[51]. Code for the modelling work is available from the corresponding authors upon request

References

1. Liu, Y., Zhu, Y. & Cui, Y. Challenges and opportunities towards fast-charging battery materials. *Nat. Energy* **4**, 540–550 (2019).
2. Masias, A., Marcicki, J. & Paxton, W. A. Opportunities and challenges of lithium ion batteries in automotive applications. *ACS Energy Lett.* **6**, 621–630 (2021).
3. Xiao, J., Shi, F., Glossmann, T., Burnett, C. & Liu, Z. From laboratory innovations to materials manufacturing for lithium-based batteries. *Nat. Energy* **8**, 329–339 (2023).
4. Wang, C. Y. et al. Fast charging of energy-dense lithium-ion batteries. *Nature* **611**, 485–490 (2022).
5. Yao, K. P. C., Okasinski, J. S., Kalaga, K., Shkrob, I. A. & Abraham, D. P. Quantifying lithium concentration gradients in the graphite electrode of Li-ion cells using: operando energy dispersive X-ray diffraction. *Energy Environ. Sci.* **12**, 656–665 (2019).
6. Finegan, D. P. et al. Spatial dynamics of lithiation and lithium plating during high-rate operation of graphite electrodes. *Energy Environ. Sci.* **13**, 2570–2584 (2020).
7. Gervillié-Mouravieff, C. et al. Unlocking cell chemistry evolution with operando fibre optic infrared spectroscopy in commercial Na(Li)-ion batteries. *Nat. Energy* **7**, 1157–1169 (2022).
8. Huang, J. et al. Operando decoding of chemical and thermal events in commercial Na(Li)-ion cells via optical sensors. *Nat. Energy* **5**, 674–683 (2020).
9. Huang, J. et al. Monitoring battery electrolyte chemistry: via in-operando tilted fiber Bragg grating sensors. *Energy Environ. Sci.* **14**, 6464–6475 (2021).
10. Liu, F. et al. Detangling electrolyte chemical dynamics in lithium sulfur batteries by operando monitoring with optical resonance combs. *Nat. Commun.* **14**, 7350 (2023).
11. Huang, J., Boles, S. T. & Tarascon, J. Sensing as the key to battery lifetime and sustainability. *Nat. Sustain.* **5**, 194–204 (2022).
12. Lu, X., Tarascon, J. M. & Huang, J. Perspective on commercializing smart sensing for batteries. *eTransportation* **14**, 100207 (2022).
13. Lu, Y. et al. Smart batteries enabled by implanted flexible sensors. *Energy Environ. Sci.* **16**, 2448–2463 (2023).
14. Deng, Z. et al. Ultrasonic scanning to observe wetting and "unwetting" in Li-ion pouch cells. *Joule* **4**, 2017–2029 (2020).
15. Louli, A. J. et al. Diagnosing and correcting anode-free cell failure via electrolyte and morphological analysis. *Nat. Energy* **5**, 693–702 (2020).
16. Zeng, Y. et al. Operando spatial mapping of lithium concentration using thermal-wave sensing. *Joule* **5**, 2195–2210 (2021).
17. Chortos, A., Liu, J. & Bao, Z. Pursuing prosthetic electronic skin. *Nat. Mater.* **15**, 937–950 (2016).
18. Hua, Q. et al. Skin-inspired highly stretchable and conformable matrix networks for multifunctional sensing. *Nat. Commun.* **9**, 244 (2018).
19. Shao, B. et al. Large-area, untethered, metamorphic, and omnidirectionally stretchable multiplexing self-powered triboelectric skins. *Nat. Commun.* **15**, 1238 (2024).
20. Zhu, S. et al. A novel embedded method for in-situ measuring internal multi-point temperatures of lithium ion batteries. *J. Power Sources* **456**, 227981 (2020).
21. Yuan, X., Liu, B., Mecklenburg, M. & Li, Y. Ultrafast deposition of faceted lithium polyhedra by outpacing SEI formation. *Nature* **620**, 86–91 (2023).
22. Fordham, A. et al. Correlative non-destructive techniques to investigate aging and orientation effects in automotive Li-ion pouch cells. *Joule* **7**, 2622–2652 (2023).
23. Nascimento, M. et al. Internal strain and temperature discrimination with optical fiber hybrid sensors in Li-ion batteries. *J. Power Sources* **410–411**, 1–9 (2019).
24. Liu, D. et al. Controlled large-area lithium deposition to reduce swelling of high-energy lithium metal pouch cells in liquid electrolytes. *Nat. Energy* **9**, 559–569 (2024).
25. Hao, S., Fu, Q., Meng, L., Xu, F. & Yang, J. A biomimetic laminated strategy enabled strain-interference free and durable flexible thermistor electronics. *Nat. Commun.* **13**, 6472 (2022).
26. Niu, S. et al. Low-temperature wearable strain sensor based on a silver nanowires/graphene composite with a near-zero temperature coefficient of resistance. *ACS Appl. Mater. Interfaces* **13**, 55307–55318 (2021).
27. Kuru, C. et al. MoS2 nanosheet–Pd nanoparticle composite for highly sensitive room temperature detection of hydrogen. *Adv. Sci.* **2**, 1500004 (2015).
28. Ridhi, R., Singh, S., Saini, G. S. S. & Tripathi, S. K. Comparison of interaction mechanisms of copper phthalocyanine and nickel phthalocyanine thin films with chemical vapours. *J. Phys. Chem. Solids* **115**, 119–126 (2018).
29. Shadman Rad, M., Danilov, D. L., Baghalha, M., Kazemeini, M. & Notten, P. H. L. Adaptive thermal modeling of Li-ion batteries. *Electrochim. Acta* **102**, 183–195 (2013).
30. Heenan, T. M. M. et al. Mapping internal temperatures during high-rate battery applications. *Nature* **617**, 507–512 (2023).
31. Huang, W. et al. Onboard early detection and mitigation of lithium plating in fast-charging batteries. *Nat. Commun.* **13**, 7091 (2022).
32. Louli, A. J., Ellis, L. D. & Dahn, J. R. Operando pressure measurements reveal solid electrolyte interphase growth to rank Li-ion cell performance. *Joule* **3**, 745–761 (2019).
33. Han, S. Y. et al. Stress evolution during cycling of alloy-anode solid-state batteries. *Joule* **5**, 2450–2465 (2021).

34. Gao, X. et al. Thermodynamic understanding of Li-dendrite formation. *Joule* **4**, 1864–1879 (2020).

35. Cao, X., Lu, Y., Song, X., Yuan, Z. & Wang, F. Perspective of unstable solid electrolyte interphase induced lithium dendrite growth: Role of thermal effect. *Electrochim. Acta* **439**, 141722 (2023).

36. Li, Y. et al. Operando decoding of surface strain in anode-free lithium metal batteries via optical fiber sensor. *Adv. Sci.* **9**, 2203247 (2022).

37. Mao, N. et al. Revealing the thermal stability and component heat contribution ratio of overcharged lithium-ion batteries during thermal runaway. *Energy* **263**, 125786 (2023).

38. Zhong, H., Zhong, Q., Yang, J. & Zhong, S. Thermal behavior and failure mechanisms of 18650 lithium ion battery induced by overcharging cycling. *Energy Rep.* **8**, 7286–7296 (2022).

39. Li, H. F., Gao, J. K. & Zhang, S. L. Effect of overdischarge on swelling and recharge performance of lithium ion cells. *Chin. J. Chem.* **26**, 1585–1588 (2008).

40. Guo, R., Lu, L., Ouyang, M. & Feng, X. Mechanism of the entire overdischarge process and overdischarge-induced internal short circuit in lithium-ion batteries. *Sci. Rep.* **6**, 30248 (2016).

41. Ma, T. et al. Degradation mechanism study and safety hazard analysis of overdischarge on commercialized lithium-ion batteries. *ACS Appl. Mater. Interfaces* **12**, 56086–56094 (2020).

42. Zhou, H., Fear, C., Carter, R. E., Love, C. T. & Mukherjee, P. P. Correlating lithium plating quantification with thermal safety characteristics of lithium-ion batteries. *Energy Storage Mater.* **66**, 103214 (2024).

43. Wang, B., Shi, J., Shi, Y., Narayanan, S. & Koratkar, N. Self-heating–induced healing of lithium dendrites. *Science* **359**, 1513–1516 (2018).

44. Kim, J., Mallarapu, A. & Santhanagopalan, S. Transport processes in a Li-ion cell during an internal short-circuit. *J. Electrochem. Soc.* **167**, 090554 (2020).

45. Feng, X., Ren, D., He, X. & Ouyang, M. Mitigating thermal runaway of lithium-ion batteries. *Joule* **4**, 743–770 (2020).

46. Vu Trung, N. et al. Tuning the thermal and mechanical properties of poly(vinyl alcohol) with 2,5-furandicarboxylic acid acting as a bio-based crosslinking agent. *Polym. J.* **54**, 335–343 (2022).

47. Ahmad, N., Wahab, R. & Al-Omar, S. Y. Thermal decomposition kinetics of sodium carboxymethyl cellulose: model-free methods. *Eur. J. Chem.* **5**, 247–251 (2014).

48. Zheng, Y., Ouyang, M., Lu, L. & Li, J. Understanding aging mechanisms in lithium-ion battery packs: from cell capacity loss to pack capacity evolution. *J. Power Sources* **278**, 287–295 (2015).

49. Lin, Y. et al. Porous enzymatic membrane for nanotextured glucose sweat sensors with high stability toward reliable noninvasive health monitoring. *Adv. Funct. Mater.* **29**, 1902521 (2019).

50. Wang, S. et al. Effects of current and ambient temperature on thermal response of lithium ion battery. *Batteries* **8**, 203 (2022).

51. Nuo S. et al. Fully printable integrated multifunctional sensor arrays for intelligent lithium-ion batteries. Zenodo, https://doi.org/10.5281/zenodo.15864165 (2024).

Acknowledgements

Author contributions

X.H. conceived the idea and supervised the work. Y.J.L. provided the framework for sensors fabrication and circuit design. N.S. and Q.L.R. performed the device fabrication, optimization, electrical measurement, sensor arrays characterization, and data analysis. N.S. and L.T.H. developed the circuit. J.W. performed SOH estimation and user interface. H.L.W. delivered the SEM and EDS characterization. J.C. contributed to the FTIR, Raman, and UV characterization. N.S. and Q.L.R. performed subject studies with the help from Y.J.L., Z.M.L., and L.Y.H. N.S. and Q.L.R. plotted the figures and wrote the first version of manuscript. K.X., S.P., Y.A.H., H.L., Y.J.L., and X.H. joined discussion and revised manuscript. All authors provided feedback on the results and the paper.

Competing interests

The authors declare no competing interests.

Additional information

Supplementary information The online version contains supplementary material available at https://doi.org/10.1038/s41467-025-62657-2.

Correspondence and requests for materials should be addressed to YongAn Huang, Kang Xu, Yuanjing Lin or Xin He.

Peer review information *Nature Communications* thanks the anonymous reviewers for their contribution to the peer review of this work. A peer review file is available.

Reprints and permissions information is available at http://www.nature.com/reprints

Publisher's note Springer Nature remains neutral with regard to jurisdictional claims in published maps and institutional affiliations.